



## CHANDRA ARCHIVAL SAMPLE OF INTRACLUSTER ENTROPY PROFILES

KENNETH. W. CAVAGNOLO<sup>1</sup>, MEGAN DONAHUE, G. MARK VOIT, AND MING SUN  
Department of Physics and Astronomy, BPS Building, Michigan State University, East Lansing, MI 48824  
*Draft version June 24, 2008*

### ABSTRACT

And he says, “Oh, uh, there won’t be any money, but when you die, on your deathbed, you will receive total consciousness.” So I got that goin’ for me, which is nice.

*Subject headings:* conduction – cooling flows – galaxies: clusters: general – X-rays: galaxies: clusters – galaxies: evolution

### 1. INTRODUCTION

The general process of galaxy cluster formation through hierarchical merging is well understood, but many details, such as the impact of feedback sources on the cluster environment and radiative cooling in the cluster core, are not. The nature of feedback operating within clusters is of great interest because of the implications for better understanding massive galaxy formation and using mass-observable scaling relations in cluster cosmological studies. Early theories of hierarchical structure formation predicted clusters of galaxies should be scaled versions of each other (Kaiser 1986; Evrard et al. 1996; Evrard 1997). These models also predicted that the most massive galaxies in the Universe – brightest cluster galaxies (BCGs) – should be rife with young stellar populations and increase in mass from their formation up to the present. However, observations have long shown that clusters do not adhere to simple, low-scatter scaling relations (Edge & Stewart 1991; Horner et al. 1999; Nevalainen et al. 2000; Finoguenov et al. 2001), and that BCGs are much lower mass systems with old stellar populations than were predicted with the theoretical models. Moreover, massive galaxies were in place by redshifts of  $\sim 1-2$  (Madau et al. 1996; Shaver et al. 1996) and have shown little sign of evolution since – the so called cosmic down-sizing problem (Cowie et al. 1996). But the problems with the theories are starting to be patched as more physics are added to hierarchical models, physics such as radiative cooling and feedback sources.

The core cooling time in many clusters is much shorter than both the Hubble time and cluster age (*e.g.* Peres et al. 1998). Thus it is reasonable to assume the cores of these clusters have gone through bouts of prodigious radiative cooling and its associated effects. One expected consequence of this radiative cooling is the formation of massive cooling flows (see Fabian 1994 for a thorough review). But, measured cooling flow mass deposition rates were found to be much lower than predicted, with the ICM never reaching temperatures lower than  $T_{\text{virial}}/3$  (Tamura et al. 2001; Peterson et al. 2001, 2003). The torrents of cool gas once thought to be flowing toward the bottom of some cluster potentials turned out to more like cooling trickles. In addition to the lack of soft X-ray line emission from cooling flows, earlier methodical searches for the end products of cooling flows (*i.e.* molecular clouds and stars) revealed far less mass was locked-up in these sources than expected (Heckman et al. 1989; McNamara et al. 1990; O’Dea et al. 1994; Voit & Donahue 1995). These disconnects between observation and theory have been termed “the cooling

flow problem” and raise the question, “Where has all the cool gas gone?” Obviously, some source of energetic feedback has heated the ICM to selectively remove gas with a short cooling time and establish quasi-stable thermal balance.

Recent revisions to models of how clusters form and evolve by including feedback sources, such as active galactic nuclei (AGN) and supernovae, has led to better agreement between observation and theory (Bower et al. 2006; Croton et al. 2006; Saro et al. 2006). The current paradigm holds that energetic feedback from AGN outbursts in the form of “bubbles” deposit the requisite heat into the ICM to retard, and in some cases quench, cooling of the ICM (see McNamara & Nulsen 2007 for a review). Thanks to the high-resolution optics aboard *Chandra*, previously unresolved ICM bubbles and cavities have indeed been observed in numerous clusters. In one of the first high-resolution X-ray studies of a sample of bubbles, ? found that AGN feedback plausible supplies the energy necessary to quench cooling in cluster cores. Many other bubble studies, including in groups and ellipticals, have come to similar conclusions.

There is yet another consequence of core cooling and secondary heating like AGN and supernovae: these processes temporarily decouple baryons in the core from the dark matter potential and give rise to the breaking of self-similarity. As a consequence of radiative cooling, best-fit total cluster temperature decreases while total cluster luminosity increases. Thus, at a given mass scale, radiative cooling conspires to create dispersion in otherwise tight correlations between mass-luminosity and mass-temperature. In addition, feedback sources can drive cluster cores (where most the cluster flux originates) away from hydrostatic equilibrium. Both of these effects result in larger uncertainties when deriving cluster masses, particularly when using mass proxies such as temperature or luminosity. This diminishes the precision desired when using clusters for detailed cosmological studies. While considerable progress has been made in this area both observationally and theoretically (Buote & Tsai 1996; Jeltema et al. 2005; Kravtsov et al. 2006; Nagai et al. 2007; Ventimiglia et al. 2008), it is still important to understand how, taken as a whole, non-gravitational processes effect cluster formation and evolution.

In this paper we present the data and results from a *Chandra* archival project in which we studied the cores of 222 galaxy clusters via their ICM entropy distributions. We have named this project the Archive of *Chandra* Cluster Entropy Profile Tables, or *ACCEPT* for short. In contrast to Donahue et al. (2006) (hereafter D06), *ACCEPT* covers a broader range of luminosities, temperatures, and morphologies, focusing on

<sup>1</sup> cavagnolo@pa.msu.edu

more than just cool core clusters. One of our primary objectives for this project was to provide the research community with an additional resource to study galaxy formation and cluster evolution. By studying ICM entropy we sought to further illuminate how cluster and BCG properties correlate with feedback activity, what can be learned of how feedback mechanisms operate, and how feedback energy is deposited in the cluster atmosphere.

Taken individually, ICM temperature and density do not fully reveal the cluster thermal history because they are most influenced by the underlying dark matter potential. Gas temperature reflects the depth of the potential well, while density reflects the capacity of the well to compress the gas. However, at constant pressure the density of a gas is determined by its specific entropy. Rewriting the expression for the adiabat,  $K = P\rho^{-5/3}$ , in terms of temperature and electron density, one can define a new quantity,  $K = Tn_e^{-2/3}$ , where  $T$  is temperature and  $n_e$  is electron gas density. This new quantity,  $K$ , captures the complete thermal history of the gas because only heating and cooling can change  $K$ . This is the quantity commonly referred to as entropy, but in actuality  $K$  is only a pseudo-entropy while the classic thermodynamic entropy is  $s = \ln K^{3/2} + \text{constant}$ .

One important property of gas entropy is that a gas cloud is convectively stable when  $dK/dr \geq 0$ . Thus, gravitational potential wells are like giant entropy sorting devices: low entropy gas sinks to the bottom of the potential well, while high entropy gas buoyantly rises to a radius of equal entropy. If a cluster were a sealed box of gravitation-only processes, then the radial entropy distribution the cluster would exhibit power-law behavior across all radii with the lowest entropy gas at the core (Voit et al. 2005). Thus, any departures of the radial entropy distribution from a power-law is indicative of additional entropy altering processes such as heating and cooling, for example from AGN.

*ACCEPT* gives us a powerful baseline to study any entropy-feedback connections which may exist. We have found that the departure of entropy profiles from a self-similar power-law, which has been discussed previously by, for example Piffaretti et al. (2005); Donahue et al. (2005, 2006); Morandi & Ettori (2007)), is not limited to cooling flow clusters, but is a feature of most clusters, and given high enough angular resolution, possibly all clusters. We have also found that indicators of feedback – namely radio sources assumed to be associated with AGN and  $H\alpha$  emission assumed to be the result of star formation in the brightest cluster galaxy (BCG) – are strongly anti-correlated with core entropy (see Cavagnolo et al. 2008a). We also find that the core entropy distribution of both the full *ACCEPT* collection and *HIFLUGCS* subsample are bimodal.

As part of this work, we are making all our work publicly available through two access points: 1) the NASA High Energy Space Archive (HEASARC) under the Chandra section of W3Browse<sup>2</sup>, and 2) our own searchable, interactive database<sup>3</sup>. At our site, the research community will find all data tables, plots, spectra, reduced *Chandra* data products (forthcoming), reduction scripts, and much more.

The structure of this paper is as follows: In §2 we outline initial sample-selection criteria and information about the *Chandra* observations selected under these criteria. Data re-

duction is discussed in §3. Spectral extraction and analysis are discussed in §3.1, while our method for deriving deprojected electron density profiles is outlined in §3.2. A few possible sources of systematics are discussed in §4. Results and discussion are presented in §5. A brief summary is given in §6. For this work we have assumed a flat  $\Lambda$ CDM Universe with cosmogony  $\Omega_M = 0.3$ ,  $\Omega_\Lambda = 0.7$ , and  $H_0 = 70 \text{ km s}^{-1} \text{ Mpc}^{-1}$ . All quoted uncertainties are 90% confidence ( $\Delta\chi^2 = 2.71$ ,  $1.6\sigma$ ). Given the large number of clusters in our sample, figures, fits, and tables showing/listing results for individual clusters have been omitted and are available at the *ACCEPT* website.

## 2. DATA COLLECTION

Our sample was initially collected from observations publicly available in the *Chandra* Data Archive (CDA) as of June 2006. We first assembled a list of targets from multiple flux-limited surveys: the *ROSAT* Brightest Cluster Sample (Ebeling et al. 1998), RBCS Extended Sample (Ebeling et al. 2000), *ROSAT* Brightest 55 Sample (Edge et al. 1990; Peres et al. 1998), *Einstein* Extended Medium Sensitivity Survey (Gioia et al. 1990), North Ecliptic Pole Survey (Henry et al. 2006), *ROSAT* Deep Cluster Survey (Rosati et al. 1995), *ROSAT* Serendipitous Survey (Vikhlinin et al. 1998), Massive Cluster Survey (Ebeling et al. 2001), and *REFLEX* Survey (Böhringer et al. 2004). After the first round of data analysis concluded, we continued to expand our collection by adding new archival data listed under the CDA Science Categories “clusters of galaxies” or “active galaxies”. As of submission, we have analyzed 491 archival observations with a pre-analysis exposure time of 16.16 Msec. The Coma and Fornax clusters have been intentionally left-out of our sample because they are very well studied nearby clusters which require a more intensive analysis than we undertook in this project.

While observations abounded, for some clusters the available data limited our ability to derive an entropy profile. Calculation of entropy requires measurement of the radial gas temperature and density structures (discussed further in §3). To infer a temperature which is reasonably well constrained ( $\pm 1.0 \text{ keV}$ ) we imposed a minimum requirement of three temperature bins containing 2500 counts each. After applying this constraint, the final sample presented in this paper has 305 observations of 222 clusters with a total exposure time of 9.58 Msec. The sample covers cluster temperatures of  $kT \sim 1 - 20 \text{ keV}$ , a bolometric luminosity range of  $L_{\text{bol}} \sim 10^{42-46} \text{ ergs s}^{-1}$ , and redshifts of  $z \sim 0.05 - 0.89$ . Table 1 lists the general properties for each cluster in *ACCEPT*.

We were unable to analyze some clusters for this study because of complications other than not meeting our minimum requirements for analysis. These clusters were: 2PIGG J0311.8-2655, 3C 129, A168, A514, A753, A1060, A1367, A2256, A2634, A2670, A2877, A3074, A3128, A3627, AS0463, APMCC 0421, MACS J2243.3-0935, MS J1621.5+2640, RX J1109.7+2145, RX J1206.6+2811, RX J1423.8+2404, SDSS J198.070267-00.984433, Triangulum Australis, and Zw5247.

We also report  $H\alpha$  observations taken by M. Donahue while a Carnegie Fellow. These observations were not utilized in this paper but are important for Cavagnolo et al. (2008a). The new  $N_{II}/H\alpha$  ratios and  $H\alpha$  fluxes are listed in Table 3. The observations were taken with either the 5 m Hale Telescope at the Palomar Observatory, USA, or the DuPont 2.5 m telescope at the Las Campanas Observatory, Chile. All observations were made with a  $2''$  slit centered on the BCG using

<sup>2</sup> <http://heasarc.gsfc.nasa.gov/W3Browse/chandra>

<sup>3</sup> <http://www.pa.msu.edu/astro/MC2/accept>

two position angles: one along the semi-major axis and one along the semi-minor axis of the galaxy. The overlap area was 10 pixels<sup>2</sup>. The red light (555-798 nm) setup on the Hale Double Spectrograph used a 316 lines/mm grating with a dispersion of 0.31 nm/pixel and an effective resolution of 0.7-0.8 nm. The DuPont Modular Spectrograph setup included a 1200 lines/mm grating with a dispersion of 0.12 nm/pixel and an effective resolution of 0.3 nm. The statistical and calibration uncertainties for the observations are both  $\sim 10\%$ . The statistical uncertainty results primarily from variability of the spectral continuum and hence imperfect background subtraction. The upper-limits listed in Table 3 are  $3\sigma$  significance.

### 3. DATA ANALYSIS

Measuring radial ICM entropy first requires measurement of radial ICM temperature and density. The radial temperature structure of each cluster was measured by fitting a single-temperature thermal model to spectra extracted from concentric annuli centered on the cluster X-ray “center”. As discussed in Cavagnolo et al. (2008b), the ICM X-ray peak of the point-source cleaned, exposure-corrected cluster image was used as the cluster center, unless the iteratively determined X-ray centroid was more than 70 kpc away from the X-ray peak in which case the centroid is used as the radial analysis zero-point. To derive the gas density profile, we first deprojected an exposure-corrected, background-subtracted, point source clean surface brightness profile extracted in the 0.7-2.0 keV energy range to attain a volume emission density. This emission density, along with spectroscopic information, was then used to convert observed surface brightness into gas density. The resulting entropy profiles were then fit with two models: a simple model which has only a radial power-law component, and a model which is the sum of a constant central entropy term,  $K_0$  and the radial power-law component.

In this paper we cover the basics of deriving gas entropy from X-ray observables, and direct interested readers to D06 for in-depth discussion of our data reprocessing and reduction, and Cavagnolo et al. (2008b) for details regarding determination of each cluster’s “center” and how the X-ray background was handled. The only difference between the analysis presented in this paper and that of D06 and Cavagnolo et al. (2008b), is that we have used newer versions of CIAO and the CALDB (CIAO 3.4.1 and CALDB 3.4.0) when reducing data for this project.

#### 3.1. Temperature Profiles

One of the two components needed to derive gas entropy is the temperature as a function of radius. We therefore constructed radial temperature profiles for each cluster in our collection. To reliably constrain a temperature and allow for the detection of temperature structure beyond simple monotonicity, we required each temperature profile to have a minimum of three annuli containing 2500 counts each. The annuli for each cluster were generated by first extracting a background-subtracted cumulative counts profile using 1 pixel width annular bins originating from the cluster center and extending to a radius bounded by the detector edge, or  $0.5R_{180}$ , whichever was smaller. Profiles were truncated at  $0.5R_{180}$  as we were most interested in the radial entropy behavior of cluster core regions ( $r \lesssim 100$  kpc) and  $0.5R_{180}$  is the approximate radius where temperature profiles turnover (Vikhlinin et al. 2005). Additionally, analysis of diffuse gas temperature structure at large radii, which spectroscopically is dominated by background, requires a time consuming, observation-specific anal-

ysis of the X-ray background (see Sun et al. 2008 for an excellent detailed discussion on this point).

Cumulative counts profiles were divided into annuli containing at least 2500 counts. For well resolved clusters, the number of counts per annulus was increased to reduce the resulting uncertainty of  $kT_X$  and, for simplicity, to keep the number of annuli less than 50. The method we use to derive entropy profiles is most sensitive to the surface brightness radial bin size and not the resolution, or uncertainties, of the temperature profile. Thus, the loss of resolution in the temperature profile from increasing the number of counts per bin, and thereby reducing the number of annuli, has an insignificant effect on the final entropy profiles and best-fit entropy models.

Background analysis was performed using the blank-sky datasets provided in the CALDB. Backgrounds were reprocessed and reprojected to match each observation. Off-axis chips were used to normalize for variations of the hard-particle background by comparing blank-sky and observation 9.5-12 keV count rates. Soft residuals were also created and fitted for each observation to account for the spatially-varying soft Galactic background. This component was added as an additional, fixed background component during spectral fitting. Errors associated with the soft background are estimated and added in quadrature to the final error.

For each radial annular region, source and background spectra were extracted from the target cluster and corresponding normalized blank-sky dataset. Using standard CIAO techniques<sup>4</sup> we created weighted response files (WARF) and redistribution matrices (WRMF) for each cluster using a flux-weighted map (WMAP) across the entire extraction region. These files quantify the effective area, quantum efficiency, and imperfect resolution of the *Chandra* instrumentation as a function of chip position. Each spectrum was binned to contain a minimum of 25 counts per energy bin.

Spectra were fitted with XSPEC 11.3.2ag (Arnaud 1996) using an absorbed, single-temperature MEKAL model (Mewe et al. 1985, 1986) over the energy range 0.7-7.0 keV. Galactic absorption values,  $N_{\text{HI}}$ , are taken from Dickey & Lockman (1990). A comparison between the  $N_{\text{HI}}$  values of Dickey & Lockman (1990) and the higher-resolution LAB Survey (Kalberla et al. 2005) reveals that the two surveys agree to within  $\pm 20\%$  for 80% of the clusters in our sample. For the other 20% of the sample, using the LAB value, or allowing  $N_{\text{HI}}$  to be free, does not result in best-fit temperatures or metallicities which differ significantly from fits using the Dickey & Lockman (1990) values.

The potentially free parameters of the absorbed thermal model are  $N_{\text{HI}}$ , X-ray temperature, metal abundance normalized to Solar (elemental ratios taken from Anders & Grevesse 1989), and a normalization proportional to the integrated emission measure within the extraction region,

$$\eta = \frac{10^{-14}}{4\pi D_A^2 (1+z)^2} \int n_e n_p dV, \quad (1)$$

where  $D_A$  is the angular diameter distance,  $z$  is cluster redshift,  $n_e$  and  $n_p$  are the electron and proton densities respectively, and  $V$  is the volume of the emission region. In all fits the metal abundance in each annulus was a free parameter and  $N_{\text{HI}}$  was fixed to the Galactic value. No systematic error is added during fitting and thus all quoted errors are statistical only. The statistic used during fitting was  $\chi^2$  (XSPEC

<sup>4</sup> <http://cxc.harvard.edu/ciao/guides/esa.html>

statistics package CHI). All uncertainties were calculated 90% confidence.

For some clusters, more than one observation was available in the archive. We utilized the combined exposure time by first extracting independent spectra, WARFs, WRMFs, normalized background spectra, and soft residuals for each observation. These independent spectra were then read into XSPEC simultaneously and fit with the same spectral model which had all parameters, except normalization, tied among the spectra.

As in D06, we find spectral deprojection does not result in significant differences between best-fit temperatures inferred for projected or deprojected quantities. Thus, for this work, we quote projected temperatures only. Deprojection of temperature should result in slightly lower temperatures in the central bins of only the clusters with the steepest temperature gradients. For these clusters, the end result would be a negligible lowering of the entropy for the central-most bins. We stress that spectral deprojection does not significantly change the shape of the entropy profiles nor the best-fit  $K_0$  values.

### 3.2. Deprojected Electron Density Profiles

For predominantly free-free emission, as is the case for the cluster ICM, gas emissivity strongly depends on gas density and only weakly on temperature,  $\epsilon \propto \rho^2 T^{1/2}$ . Therefore the measured flux in a narrow temperature range is an excellent measure of ICM density. To reconstruct the relevant gas density as a function of physical radius we deprojected the cluster emission from high-resolution surface brightness profiles and converted to electron density using normalizations and count rates taken from the spectral analysis.

We extracted surface brightness profiles from the 0.7-2.0 keV energy range (where the bulk of cluster emission occurs) using concentric annular bins of size  $5''$  (10 ACIS pixels) originating from the cluster center. Each surface brightness profile was corrected with an observation specific, normalized radial exposure profile to remove the effects of vignetting and exposure time fluctuations. Following the recommendation in the CIAO guide for analyzing extended sources, exposure maps were created using the monoenergetic value associated with the observed count rate peak. The more sophisticated method of creating exposure maps using spectral weights calculated for an incident spectrum with the temperature and metallicity of the observed cluster was also tested. For the narrow energy band we consider, the chip response is relatively flat and we find no significant differences between the two methods. For all clusters the monoenergetic value was between 0.8–1.7 keV.

The 0.7-2.0 keV spectroscopic count rate and spectral normalization were interpolated from the radial temperature profile grid to match the surface brightness radial grid. Utilizing the deprojection technique of Kriss et al. (1983), the interpolated spectral parameters were used to convert observed surface brightness to deprojected electron density. Radial electron density written in terms of relevant quantities is,

$$n_e(r) = \sqrt{\frac{1.2 \cdot 4\pi [D_A(1+z)]^2 C(r) \eta(r)}{10^{-14} f(r)}} \quad (2)$$

where 1.2 is an ionization ratio ( $n_e = 1.2 n_p$ ),  $C(r)$  is the radial emission density derived from Eqn. A1 in Kriss et al. (1983),  $\eta$  is the interpolated spectral normalization from Eqn. 1,  $D_A$  is the angular diameter distance,  $z$  is cluster redshift, and  $f(r)$  is the interpolated spectroscopic count rate. Cosmic reddening

of source surface brightness is accounted for by the  $D_A^2(1+z)^2$  term. This method of deprojection takes into account temperature and metallicity fluctuations which affect observed gas emissivity. Errors for the gas density profile were estimated using 5000 Monte Carlo simulations of the original surface brightness profile. This deprojection technique requires an assumption of spatial symmetry, and while we only consider spherical symmetry, it was shown in Donahue et al. (2006) that this assumption has little effect on our results.

### 3.3. $\beta$ -model Fits

Noisy surface brightness profiles, or profiles with irregularities such as inversions or extended flat cores, result in unstable, unphysical quantities when using the “onion” deprojection technique. For cases where deprojection of the raw data was problematic, we resorted to fitting the surface brightness profile with a  $\beta$ -model (Cavaliere & Fusco-Femiano 1978). It is well known that the  $\beta$ -model is only an approximation for an isothermal gas distribution and does not precisely represent all the features of the ICM (Ettori 2000; Loken et al. 2002; Hallman et al. 2007). However, for the profiles we found required a fit, the  $\beta$ -model is a suitable approximation, and the models use is only a means for creating a smooth function which is easily deprojected. The single ( $N = 1$ ) and double ( $N = 2$ )  $\beta$ -models were used in fitting,

$$S_X = \sum_{i=1}^N S_i \left[ 1 + \left( \frac{r}{r_{c,i}} \right)^2 \right]^{-3\beta_i + \frac{1}{2}}. \quad (3)$$

The models were fitted using Craig Markwardt’s robust non-linear least squares minimization IDL routines<sup>5</sup>. The data input to the fitting routines were weighted using the inverse square of the observational errors. Using this weighting scheme resulted in residuals which were near unity for, on average, the inner 80% of the radial range considered. Accuracy of errors output from the fitting routine were checked against a bootstrap Monte Carlo analysis of 1000 surface brightness realizations. Both the single- and double- $\beta$  models were fit to each profile and we established which model best represented the surface brightness profile by making a model comparison via an F-test.

A best-fit  $\beta$ -model was used in place of the data when deriving electron density for the clusters listed in Table 2. These clusters are also flagged in Table 1 with the note letter ‘a’. The best-fit  $\beta$ -models and background-subtracted, exposure-corrected surface brightness profiles are shown in Figure 1 and the parameters are given in Table ?? . See Appendix A for notes discussing individual clusters. The disagreement between the best-fit  $\beta$ -model and the surface brightness in the central regions for some clusters is also discussed in Appendix A. In short, the discrepancy arises from the presence of compact X-ray sources, a topic which is addressed in §3.5. All clusters requiring a  $\beta$ -model fit have  $K_0 > 95 \text{ keV cm}^2$  with a mean  $K_0 = 232 \pm 77 \text{ keV cm}^2$ .

### 3.4. Entropy Profiles

Radial entropy profiles were calculated using the widely adopted formulation  $K(r) = T(r)n_e(r)^{-2/3}$  Lloyd-Davies et al. (2000). To create the radial entropy profiles, the temperature and density profiles must be on the same radial grid. This was accomplished by interpolating the temperature profile across

<sup>5</sup> available at <http://cow.physics.wisc.edu/~craigm/idl/>

the higher-resolution radial grid of the deprojected electron density profile. In general, the higher radial resolution of the density profiles means that the central bin of the temperature profile spans several bins of the density profile. Since we are most interested in the behavior of the entropy profiles in the central regions, how the interpolation was performed in this part of the profiles was important. Thus, temperature interpolation over the region of the density profile where a single temperature bin encompasses several central density bins was applied in two ways: 1) as a linear gradient consistent with the slope of the temperature profile at radii larger than the central  $T_X$  bin ( $\Delta T_{center} \neq 0$ ), and 2) as a constant ( $\Delta T_{center} = 0$ ). Shown in Figure 2 is the ratio of best-fit core entropy,  $K_0$ , derived using the above two methods. The five points lying below the line of equality are clusters which are best-fit by a power-law or have  $K_0$  statistically consistent with zero. It is worth noting that both schemes yield statistically consistent values for  $K_0$  except for the clusters marked by red points which have a ratio significantly different from unity.

These special cases all have steep temperature gradients with the maximum and minimum radial temperatures differing by a factor of 1.3-5.0. Extrapolation of a steep temperature gradient as  $r \rightarrow 0$  results in very low central temperatures (typically  $T_X \leq T_{virial}/3$ ) which are inconsistent with observations, most notably Peterson et al. (2003). Most important however, is that the flattening of entropy we observe in the cores of our sample (discussed in §5.1) is *not* a result of the method chosen for interpolating the temperature profile. For this paper we therefore focus on the results derived assuming a constant temperature across the central-most bins.

Uncertainty in  $K(r)$  arising from assuming gas inhomogeneity contributes negligibly to our final fits, *e.g.* assuming gas within an annular region is best described by a single temperature model, is discussed in detail in the Appendix of D06. Briefly summarizing D06: we have primarily measured the entropy of the lowest entropy gas because it is the most luminous gas. For the best-fit entropy values to be significantly changed, the volume filling fraction of a higher-entropy component must be non-trivial ( $> 50\%$ ). As discussed in D06, our results are robust to the presence of multiple, low luminosity gas phases and mostly insensitive to X-ray surface brightness decrements, such as X-ray cavities and bubbles, although in extreme cases their influence on an entropy profile can be detected (for an example see the cluster A2052).

Each entropy profile was fit with two models: (1) a simple model which is a power-law at large radii and approaches a constant value at small radii, and (2) a model which is a power-law only:

$$(1) K(r) = K_0 + K_{100} \left( \frac{r}{100 \text{ kpc}} \right)^\alpha$$

$$(2) K(r) = K_{100} \left( \frac{r}{100 \text{ kpc}} \right)^\alpha.$$

In these models,  $K_0$  is what we call core entropy,  $K_{100}$  is a normalization for entropy at 100 kpc, and  $\alpha$  is the power-law index. Note, however, that  $K_0$  does not necessarily represent the minimum core entropy or the entropy at  $r = 0$ . Nor does  $K_0$  capture the gas entropy which would be measured immediately around an AGN or in a BCG X-ray coronae. Instead,  $K_0$  represents the typical excess of core entropy above the best fitting power-law found at larger radii. Fits were truncated at a maximum radius (determined by-eye) to avoid the influence of noisy bins at large radii which result from instability of our

deprojection method. A listing of all the best-fit parameters for each cluster are published at the *ACCEPT* website.

Some clusters have a surface brightness profile which is comparable to a double  $\beta$ -model. Our models for the behavior of  $K(r)$  are intentionally simplistic and are not intended to fully describe all the features of  $K(r)$ . Thus, for the small number of clusters with discernible double- $\beta$  behavior, fitting of the entropy profiles was restricted to the innermost of the two  $\beta$ -like features. These clusters have been flagged in Table 1 with the note letter 'b'. The best-fit power-law index is typically much steeper for these clusters, but the outer regions, which we do not discuss here, have power-law indices which are typical of the rest of the sample, *i.e.*  $\alpha \sim 1.2$ .

### 3.5. Exclusion of Central Sources

For many clusters in our sample the ICM X-ray peak, ICM X-ray centroid, optical BCG emission, and infrared BCG emission are coincident or well within 70 kpc of one another. This made identification of the cluster center robust and trivial. However, in some clusters, there is an X-ray point source or compact X-ray source ( $r \lesssim 5$  kpc) found very near ( $r < 10$  kpc) the cluster center and always associated with a BCG. For some clusters – such as 3C 295, A2052, A426, Cygnus A, Hydra A, or M87 – the source is an AGN and there was no question the source must be removed.

However, determining how to handle the compact X-ray sources was not so straight-forward. These compact sources are larger than the PSF, fainter than an AGN, but are typically more luminous than the surrounding ICM such that the compact source's extent was distinguishable from the ICM. These sources are most prominent, and thus the most troublesome, in non-cool core clusters (*i.e.* clusters which are mostly isothermal). They are troublesome because the compact source is typically much cooler and denser than the surrounding ICM and hence has an entropy much lower than the ambient ICM. We suspect most of these compact sources are X-ray coronae (Sun et al. 2007), although they may be something else as we have not studied them in detail yet.

After deriving radial entropy profiles for clusters with a compact source at the center, without removing the source, we found  $K(r)$  abruptly declines when the outer edge of the compact source is reached (typically only one or two central surface brightness bins). This discontinuity in  $K(r)$  means the simple models we used for fitting  $K(r)$  no longer were a good description of the profile. Obviously, two solutions were available: exclude or keep the compact sources during analysis. Including the compact sources results in the central cluster region(s) appearing overdense, and at a given temperature the region will be lower entropy than if the source were excluded. Aside from producing poor fits, this significantly lower entropy influences the value of best-fit parameters because the shape of  $K(r)$  is drastically changed. Deciding what to do with these sources depends upon what cluster properties we specifically are interested in quantifying.

Simply put, the compact X-ray sources discussed in this section are not representative of the cluster's core entropy; these sources are representative of the entropy within and immediately surrounding the BCG – which is not the quantity we are interested in measuring at this time. Our focus in this work was to quantify the entropy structure of the cluster core region, not to determine the minimum entropy of cluster cores or to quantify the entropy of peculiar core objects such as BCG coronae. Thus, we decided to exclude these compact sources during our analysis.

**[Do I want to add an appendix for... Notes regarding individual clusters/sources are provided in Appendix ??.]**

For most compact sources, the exclusion region used had an area which was  $< 10\%$  of the central surface brightness bin area. For a few extraordinary sources the central one to two bins of the surface brightness profile were ignored during analysis **[Which clusters? Flag them.]** The 28 clusters which had a central source removed have been flagged in Table 1 with the note letter 'd' for AGN and 'e' for compact sources. The mean best-fit parameters for these clusters are  $K_0 = 39.5 \pm 16.6 \text{ keV cm}^2$ ,  $\alpha = 1.22 \pm 0.39$ , and  $K_{100} = 140 \pm 47 \text{ keV cm}^2$ . These clusters cover the redshift range  $z = 0.0044 - 0.4641$  with mean  $z = 0.1196 \pm 0.1234$ , and temperature range  $kT_X = 1 - 12 \text{ keV}$  with mean  $kT_X = 4.43 \pm 2.53 \text{ keV}$ . Dividing these clusters into two subgroups, those above and below  $K_0 = 50 \text{ keV cm}^2$ , the means for clusters with  $K_0 < 50 \text{ keV cm}^2$  are  $K_0 = 15.6 \pm 5.2 \text{ keV cm}^2$ ,  $\alpha = 1.16 \pm 0.38$ , and  $K_{100} = 146 \pm 48 \text{ keV cm}^2$ . For clusters with  $K_0 > 50 \text{ keV cm}^2$  the means are  $K_0 = 136 \pm 44 \text{ keV cm}^2$ ,  $\alpha = 1.33 \pm 0.44$ , and  $K_{100} = 122 \pm 45 \text{ keV cm}^2$ . The range and mean of the redshifts and temperatures for the two subgroups are not significantly different.

It is worth noting that when any source is excluded from the data, the empty pixels where the source once was are not included in the calculation of the surface brightness (counts and pixels are both excluded). Thus, the decrease in surface brightness of a bin where a source has been removed is not a result of the count to area ratio being artificially reduced.

#### 4. SYSTEMATICS

Our models for  $K(r)$  were created so the best-fit  $K_0$  values take on the definition of being a good measure of the entropy profile flattening at small radii. There is the possibility that this flattening may be exaggerated or reduced through the effects of systematics such as PSF smearing and surface brightness profile angular resolution. To quantify the extent to which our  $K_0$  values are being affected by these systematics, we have analyzed mock *Chandra* observations created using the ray-tracing program MARX<sup>6</sup>, and also by analyzing degraded entropy profiles generated from artificially redshifting well-resolved clusters.

##### 4.1. PSF Effects

To assess the effect of PSF smearing on our entropy profiles we have updated the analysis presented in §4.1 of D06 to include MARX simulations. In the D06 analysis we assumed the density and temperature structure of the cluster core obeyed power-laws with  $n_e \propto r^{-1}$  and  $T_X \propto r^{1/3}$ . This results in a power-law entropy profile with  $K \propto r$ . Further assuming the main emission mechanism is thermal Bremsstrahlung, *i.e.*  $\epsilon_X \propto T_X^{1/2}$ , yields a surface brightness profile which has the form  $S_X \propto r^{-5/6}$ . A source image consistent with these parameters was created in IDL and then input to MARX to create the mock *Chandra* observations.

The MARX simulations were performed using the spectrum of a 4.0 keV, 0.3 $Z_\odot$  abundance MEKAL model. We have tested using input spectra with  $kT = 2 - 10 \text{ keV}$  with varying abundances and find the effect of temperature and metallicity on the distribution of photons in MARX to be insignificant for our discussion here. We have neglected the X-ray background in this analysis as it is overwhelmed by cluster emission in the

core and is only important at large radii. Observations for both ACIS-S and ACIS-I instruments were simulated using an exposure time of 40 ksec. A surface brightness profile was then extracted from the mock observations using the same  $5''$  bins used on the real data.

For  $5''$  bins, we find the difference between the central bins of the input surface brightness and the output MARX observation to be less than the statistical uncertainty. The on-axis *Chandra* PSF is  $\lesssim 1''$  and the surface brightness bins we have used on the data are five times this size. Our analysis using MARX bears out that PSF effects are negligible in our study because the data bins are so much larger than the PSF. Most interesting and important though, is that our analysis using MARX suggests any deviation of the surface brightness – and consequently the entropy profile – from a power-law, even if only in the central bin, is real and cannot be attributed to PSF effects. Even for the most poorly resolved clusters, the deviation away from a power-law we observe in so many of our entropy profiles is not an artifact of the data analysis or deprojection technique.

##### 4.2. Angular Resolution Effects

Another possible limitation on evaluating  $K_0$  is the effect of using fixed angular size bins for extracting surface brightness profiles. This choice may introduce a redshift-dependence into the best-fit  $K_0$  values because as redshift increases, a fixed angular size encompasses a larger physical volume and the value of  $K_0$  may increase if the bin includes a broad range of gas entropy. Shown in Figure 3 is a plot of the best-fit  $K_0$  values for our entire sample versus redshift. Above  $K_0 \approx 10 \text{ keV cm}^2$ , our sample is fairly complete at all redshifts **[How to quantify this?]**. However, at the lowest redshifts ( $z < 0.02$ ), there are a few objects with  $K_0 < 10 \text{ keV cm}^2$  and only one at higher redshifts (A1991 –  $K_0 = 1.53 \pm 0.32$ ,  $z = 0.0587$  – which is a very peculiar cluster (Sharma et al. 2004)). This raises the question: can the lack of clusters with  $K_0 \lesssim 10 \text{ keV cm}^2$  at  $z > 0.02$  be completely explained by resolution effects?

To answer this question we tested the effect redshift has on measuring  $K_0$  by selecting all clusters with  $K_0 \leq 10 \text{ keV cm}^2$  and  $z \leq 0.1$  and degrading their surface brightness profiles to mimic the effect of increasing the cluster redshift. Our test is best illustrated using an example: first, consider a cluster at  $z = 0.1$ . For this cluster,  $5''$  equals 9 kpc. Were the cluster at  $z = 0.2$ ,  $5''$  would equal 16 kpc. To mimic moving this example cluster from  $z = 0.1 \rightarrow 0.2$ , we can extract a new surface brightness profile using a bin size of 16 kpc instead of  $5''$ . This will result in a new surface brightness profile which has the angular resolution for a cluster at a higher redshift. This is the procedure we used for degrading the profiles of our subsample. This process of calculating new bin sizes to artificially redshift clusters was repeated over an evenly distributed grid of redshifts in the range  $z = 0.1 - 0.4$  using step sizes of 0.02. The temperature profiles for each cluster were also degraded by starting at the innermost temperature profile annulus and pairing-up neighboring annuli moving outward. New spectra were extracted for these enlarged regions and analyzed following the same procedure detailed in §3.1.

The ensemble of artificially redshifted clusters was then analyzed using the procedure detailed in §3.4. There are a few notable effects on the entropy profiles arising from lower angular resolution. Obviously, as redshift increases, the number of radial bins decreases. The resulting effect is that detail of the entropy profile's curvature is diminished, *e.g.* the pro-

<sup>6</sup> <http://space.mit.edu/CXC/MARX/>



files become straighter. On its own this effect should lead to lower best-fit  $K_0$  values, but, while profile curvature is reduced, the entropy of the central-most bins is increasing because they encompass a broader range of entropy. From  $z = 0.1 - 0.2$  this last effect dominates, resulting in an increase of  $(K'_0 - K_0)/K_0 \approx [XX] - [YY]$  **[Is this really how I want to quantify this?]**. However, at  $z > 0.2$ , too much radial resolution is lost and the degraded profiles begin to resemble power-laws except in the innermost bin which still lies above the power-law (this however is accompanied by a large increase of the uncertainty in  $K_0$ ). The result of a power-law profile with a discrepant central bin is that the degraded  $K_0$  values are only slightly larger than the original  $K_0$ ,  $(K'_0 - K_0)/K_0 \approx [XX] - [YY]$  **[Missing data]**, but have much larger uncertainties.

Our analysis of the degraded entropy profiles suggests that  $K_0$  is more sensitive to the value of  $K(r)$  in the central bins than it is to the shape of the profile or the number of radial bins (results we discuss further in §4.3). Most importantly however is that low-redshift clusters with  $K_0$  values in the range  $2 - 10 \text{ keV cm}^2$  look like  $K_0 \approx 10 - 25 \text{ keV cm}^2$  clusters at  $z > 0.1$ . Thus we conclude that the lack of  $K_0 < 10 \text{ keV cm}^2$  clusters at  $z \gtrsim 0.1$  can be attributed to resolution effects.

#### 4.3. Profile Curvature and Number of Bins

In the previous section, our analysis of degraded entropy profiles illuminated two concerning points: 1) that  $K_0$  is sensitive to the curvature of the entropy profile, and 2) that the number of radial bins also effects the best-fit  $K_0$ . This raises the possibility of two troubling systematics in our analysis. To evaluate the dependence of  $K_0$  on profile curvature we first calculated average profile curvatures,  $\kappa_A$ . For each profile  $\kappa_A$  was calculated using the standard formulation  $\kappa = \|y''\|/(1+y'^2)^{3/2}$ , where for our application  $y = K(r) = K_0 + K_{100}(r/100 \text{ kpc})^\alpha$ , yielding:

$$\kappa_A = \frac{1}{\int dr} \int \frac{\|100^{-\alpha}(\alpha-1)\alpha K_{100}r^{\alpha-2}\|}{[1+(100^{-\alpha}\alpha K_{100}r^{\alpha-1})^2]^{3/2}} \quad (4)$$

where  $\alpha$  and  $K_{100}$  are the best-fit parameters unique to each entropy profile. We find that at any value of  $K_0$  a large range of curvatures are covered and that there is no underlying systematic trend in  $K_0$  associated with curvature.

In §4.2 we found that profiles with fewer radial bins tend toward lower best-fit  $K_0$  values. After examining plots of the number of bins fit in each entropy profile versus  $K_0$  we find only scatter and no trends. The radial resolution effect on  $K_0$  we found in the degraded profiles is not present in the real data.

We do not find any systematic trends with profile shape or number of fit bins which would significantly effect our best-fit  $K_0$  values. Thus we conclude that the  $K_0$  values presented in the following sections are an excellent measure of the core entropy and any undetected dependence on profile shape or radial resolution effect our results at significance levels much smaller than the measured uncertainties.

### 5. RESULTS AND DISCUSSION

Presented in Figure 4 is a montage of *ACCEPT* entropy profiles for different temperature ranges. These figures highlight the cornerstone result of *ACCEPT*: a uniformly analyzed collection of entropy profiles covering a broad range of core entropy. Each profile is color-coded in representation of the global cluster temperature. Also plotted in the figure is the

“baseline” entropy profile calculated by Voit et al. (2005). This theoretical curve represents the entropy profile of self-similar clusters without feedback and for which the radial entropy profile scales linearly with cluster temperature. This profile ignores the effects of non-gravitational processes and thus gives a lower-limit with which we can compare our profiles.

In the following sections we discuss the results gleaned from analysis of our library of entropy profiles. Results such as the departure of most entropy profiles from a simple radial power-law profile, the bimodal distribution of core entropy, and the asymptotic convergence of the entropy profiles to the self-similar  $K(r) \propto r^{1.1}$  power-law at  $r \geq 100 \text{ kpc}$ .

#### 5.1. Non-Zero Core Entropy

Arguably the most striking feature of Figure 4 is the departure of most profiles from a simple power-law. Flattening of surface brightness profiles (and conversely ICM gas density) is a well known feature of clusters (e.g. Mohr et al. 1999, Xue & Wu 2000, and references therein). What is notable in our work however is that, based on comparison of reduced  $\chi^2$ , very few of the clusters in our sample have an entropy distribution which is best-fit by the power-law only model.

Of the 222 in *ACCEPT*, only four clusters have a  $K_0$  value which is statistically consistent with zero, or are better fit by the power-law only model: A2151, AS0405, MS 0116.3-0115, and NGC 507 (used during analysis of *HIFLUGCS* sample only). Two clusters, A1991 and A4059, are better fit by the power-law model when the temperature profile in the core is not constant (see §3.1). For these six clusters it may be the case that the ICM entropy departs from a power-law at a radial scale smaller than the  $5''$  bins we used for extracting surface brightness profiles. After extracting new surface brightness profiles for these six clusters using  $2.5''$  bins and repeating the analysis, we find that the profiles for A4059 and AS0405 do flatten. This leaves A1919, A2151, MS 0116.3-0115, and NGC 507 as the only clusters in *ACCEPT* which are statistically best-fit by power-laws.

For the entire sample, the mean  $K_0 = 71.1 \pm 32.9 \text{ keV cm}^2$ . Subdividing the collection into two categories – clusters with  $K_0$  below and above  $50 \text{ keV cm}^2$  – we find means of  $K_0 = 16.0 \pm 5.7 \text{ keV cm}^2$  and  $K_0 = 154 \pm 53 \text{ keV cm}^2$ , respectively. We show in the following section, §5.2, that the cut at  $K_0 = 50 \text{ keV cm}^2$  is not completely arbitrary.

For clusters with central cooling times shorter than the age of the cluster, non-zero core entropy is an expected consequence of episodic heating of the ICM (David et al. 2001; Kaiser & Binney 2003), with AGN as one possible heating source (see Voit & Donahue 2005 as an example feedback model and McNamara & Nulsen 2007 for a review). Clusters with cooling times of order the age of the Universe, however, require other mechanisms to generate their core entropy, for example via mergers or extremely energetic AGN outbursts. For the very highest  $K_0$  values,  $K_0 > 100 \text{ keV cm}^2$ , the mechanism by which the core entropy of these clusters came to be so large is not well understood as it is difficult to boost the entropy of a gas parcel to  $> 100 \text{ keV cm}^2$  via merger shocks (McCarthy et al. 2008) or requires unsubstantiated AGN outburst energies. We have provided the data within *ACCEPT* to the public with the hope that it provides the research community a new resource to further understand the processes which result in non-zero cluster core entropy.

#### 5.2. Bimodality of Core Entropy Distribution

The time required for a gas parcel to radiate away its thermal energy is a function of the gas entropy. Low entropy gas radiates profusely and is thus subject to rapid cooling and vice versa for high entropy gas. Thus, the distribution of  $K_0$  is of particular interest because it is an approximate indicator of the cooling timescale in the cluster core. The  $K_0$  distribution is also interesting because it may be useful in better understanding the physical processes operating in cluster cores. For example, if processes such as thermal conduction and AGN feedback are important in establishing the entropy state of cluster cores, then models which incorporate these processes should approximately reproduce the observed  $K_0$  distribution.

In the top panel of Figure 5 is plotted the logarithmically binned distribution of  $K_0$ . In the bottom panel of Figure 5 is plotted the cumulative distribution of  $K_0$ . One can immediately see from these distributions that there are at least two distinct populations separated by a small number of clusters with  $K_0 \approx 40 - 60 \text{ keV cm}^2$ . If the distinct bimodality of the  $K_0$  distribution seen in the binned histogram were an artifact of binning, then the cumulative distribution should be relatively smooth. But there are clearly plateaus in the cumulative distribution, with one of these plateaus coincident with the division between the two populations at  $K_0 \approx 40 - 60 \text{ keV cm}^2$ .

To further test for the presence of a bimodal population we utilized the KMM test of Ashman et al. (1994). The KMM test estimates the probability that a set of data points is better described by the sum of multiple Gaussians than by a single Gaussian. We tested the unimodal case versus the bimodal case with the assumption that the dispersion of the two Gaussian components are not the same (*e.g.* the heteroscedastic case). We have used the updated KMM code of Waters et al. 2008 (ApJ, in press) which incorporates bootstrap resampling to determine uncertainties for all parameters. A post-analysis comparison of the hetero- and homoscedastic cases confirms that our initial guess that the heteroscedastic case is a better model.

The KMM test, as with any statistical test, is very specific. At zeroth order, the KMM test simply determines if a population is bimodal or not. The KMM test also reliably finds the means of these populations. However, the dispersions of these populations are subject to the quality of sampling and the presence of outliers (*e.g.* KMM must assign all data points to a population). The output of the KMM test are the best-fit populations to the data, not necessarily the best-fit populations of the underlying distribution (hence no goodness of fit is output).

There are a small number of clusters with  $K_0 \leq 4 \text{ keV cm}^2$  that when included in the KMM test significantly change the results. Thus we provide two sets of results: results with and without the  $K_0 \leq 4 \text{ keV cm}^2$  clusters. The results of the KMM test neglecting  $K_0 \leq 4 \text{ keV cm}^2$  clusters were two statistically distinct peaks at  $K_1 = 17.8 \pm 6.6 \text{ keV cm}^2$  and  $K_2 = 154 \pm 52 \text{ keV cm}^2$ . 118 clusters were assigned to the first distribution, while 104 were assigned to the second. Including  $K_0 \leq 4 \text{ keV cm}^2$  clusters, the KMM test found populations at  $K_1 = 15.0 \pm 5.0 \text{ keV cm}^2$  (87 clusters) and  $K_2 = 129 \pm 45 \text{ keV cm}^2$  (126 clusters). The KMM test also outputs a P-value,  $p$ , and with the assumption that  $\chi^2$  describes the distribution of the likelihood ratio statistic,  $1 - p$  is the confidence interval for the model considered. The KMM test neglecting  $K_0 \leq 4 \text{ keV cm}^2$  clusters returned  $p = 1.16 \times 10^{-7}$ , while the test including all clusters returned  $p = 1.90 \times 10^{-13}$ . These tiny  $p$ -values indicate the probability the  $K_0$  distribution we observe in our data arises from a single population is

astoundingly remote.

One explanation for the bimodal entropy distribution is that it arises from the effects of episodic AGN feedback and electron thermal conduction in the cluster core. Voit & Donahue (2005) put forth a model of AGN induced heating of the ICM whereby outbursts of  $\sim 10^{45} \text{ ergs s}^{-1}$  occurring every  $\sim 10^8 \text{ yrs}$  can maintain a quasi-steady core entropy of  $\approx 10 - 30 \text{ keV cm}^2$ . In addition, very energetic and infrequent AGN outbursts of  $10^{61} \text{ ergs}$  can increase the core entropy into the  $\approx 30 - 50 \text{ keV cm}^2$  range. This model predicts quite well the distribution at  $K_0 \lesssim 50 \text{ keV cm}^2$ , but depletion of the  $K_0 = 40 - 60 \text{ keV cm}^2$  region and populating  $K_0 > 60 \text{ keV cm}^2$  requires more physics. Voit et al. (2008) have recently suggested that the dramatic fall-off of clusters beginning at  $K_0 \approx 30 \text{ keV cm}^2$  may be the result of heat input via electron thermal conduction overtaking energy losses via radiative cooling thus preventing, or at least severely slowing, a cluster's core from appreciably cooling and returning to a core entropy state below  $K_0 > 30 \text{ keV cm}^2$ .

One consequence of these proposed models is that thermal instabilities resulting from inefficient conduction should preferentially, but not exclusively, form only below an entropy threshold where conduction and cooling are balanced. These thermal instabilities may then result in various by-products, such as star formation and AGN. If so, then indicators of these feedback sources being active (such as H $\alpha$  emission or radio emission from the BCG) would be sensitive to and entropy threshold. In Cavagnolo et al. (2008a) we show that indeed H $\alpha$  and powerful radio emission ( $\nu L_\nu > 10^{40} \text{ ergs s}^{-1}$ ) are predominantly detected for BCGs residing in clusters with  $K_0 \lesssim 30 \text{ keV cm}^2$ , while above  $K_0 = 30 \text{ keV cm}^2$  H $\alpha$  is not detected and when radio emission is detected, it is extremely faint ( $\nu L_\nu < 10^{40} \text{ ergs s}^{-1}$ ). Our speculation regarding the origins of bimodality are further bolstered by the recent theoretical work of Guo et al. (2008) which shows that a combination of AGN feedback and conduction are capable of preventing the formation of thermal instabilities in cluster cores. The recent observational work of Rafferty et al. (2008) which finds blue gradients only for BCGs in clusters with  $K_0 \lesssim 30 \text{ keV cm}^2$  is an additional piece of evidence that conduction may be important.

We acknowledge that *ACCEPT* is not a complete, uniformly selected sample of clusters. This raises the possibility that our sample is biased, possibly towards clusters that have historically drawn the attention of observers, such as cooling flows or mergers. If that were the case, then one reasonable explanation of the  $K_0$  bimodality is that  $K_0 = 30 - 60 \text{ keV cm}^2$  clusters are “boring” and thus go unobserved. However, as we show in §5.4, the unbiased flux-limited *HIFLUGCS* sample is also bimodal. A sociological explanation of bimodality for both *ACCEPT* and *HIFLUGCS* is highly unlikely.

### 5.3. The *HIFLUGCS* Sub-Sample

The clusters comprising *ACCEPT* were not selected using any well-defined criteria. To ensure our results are not affected by an unknown selection bias, we culled the Highest X-Ray Flux Galaxy Cluster Sample (*HIFLUGCS*, Reiprich 2001; Reiprich & Böhringer 2002) from *ACCEPT* for analysis. *HIFLUGCS* is a flux-limited sample ( $f_X \geq 2 \times 10^{-11} \text{ ergs s}^{-1} \text{ cm}^{-2}$ ) of objects selected by flux only from the *REFLEX* sample (Böhringer et al. 2004) with no consideration of morphology. Thus, at any given luminosity in *HIFLUGCS* there is a good sampling of different morphologies, *i.e.* the bias toward cool-cores or mergers has been removed.



The sample also covers most of the sky with holes near Virgo and the Large and Small Magellanic Clouds. The sample also has no known incompleteness (Chen et al. 2007). There are a total of 106 objects in *HIFLUGCS*: 63 in the primary sample and 43 in the extended sample. Of these 106 objects, no public *Chandra* observations were available for 16 objects (A548e, A548w, A1775, A1800, A3528n, A3530, A3532, A3560, A3695, A3827, A3888, AS0636, HCG 94, IC 1365, NGC 499, RXCJ 2344.2-0422), ten objects did not meet our minimum analysis requirements and were thus insufficient for study (3C 129, A400, A1060, A1367, A2256, A2634, A2877, A3627, MKW 08, Triangulum Australis), and as discussed in §2, Coma and Fornax were intentionally ignored. This left a total of 78 *HIFLUGCS* objects which we analyzed, 57 from the primary sample and 23 from the extended sample. The primary sample is the most complete of the two, thus we focus our following discussion on the primary sample only.

As shown in Figure 6, the bimodality seen in the full *ACCEPT* collection is also present in the *HIFLUGCS* subsample. Dividing the clusters into those below and above  $K_0 = 50 \text{ keV cm}^2$ , the mean parameters are  $\alpha = 1.19 \pm 0.38$ ,  $K_0 = 11.8 \pm 4.3 \text{ keV cm}^2$ ,  $K_{100} = 241 \pm 92 \text{ keV cm}^2$ , and  $\alpha = 1.15 \pm 0.38 \text{ keV cm}^2$ ,  $K_0 = 149 \pm 52 \text{ keV cm}^2$ ,  $K_{100} = 116 \pm 42 \text{ keV cm}^2$ , respectively. We again performed two KMM tests, one with another without clusters having  $K_0 \leq 4 \text{ keV cm}^2$ . For the test including  $K_0 \leq 4 \text{ keV cm}^2$  clusters we find populations at  $K_1 = 10.4 \pm 3.8 \text{ keV cm}^2$  (28 clusters) and  $K_2 = 133 \pm 46 \text{ keV cm}^2$  (28 clusters with  $p = 5.13 \times 10^{-3}$ ). Excluding clusters with  $K_0 \leq 4 \text{ keV cm}^2$  we find peaks at  $K_1 = 10.8 \pm 3.5 \text{ keV cm}^2$  and  $K_2 = 112 \pm 40 \text{ keV cm}^2$  each having 21 and 31 clusters, respectively. The probability these populations originate from a unimodal distribution is  $p = 3.21 \times 10^{-6}$ . It is interesting that the gap in the  $K_0$  distributions for *ACCEPT* and *HIFLUGCS* occur in the same location,  $K_0 \approx 40 - 60 \text{ keV cm}^2$ . That bimodality is present in both *ACCEPT* and the unbiased *HIFLUGCS* subsample suggests bimodality cannot be the result of simple archival bias.

In a conference proceeding, Hudson & Reiprich (2007) note a similar core entropy bimodality for the *HIFLUGCS* sample as the one we find here. Hudson & Reiprich (2007) discuss two distinct groupings of objects in a plot of average cluster temperature versus core entropy, with the dividing point being  $K \approx 40 \text{ keV cm}^2$ . Our results agree with the findings of Hudson & Reiprich (2007) with the gap in  $K_0$  occurring around  $K_0 = 40 \text{ keV cm}^2$ .

#### 5.4. Distribution of Core Cooling Times

In the X-ray regime, cooling time and entropy are related in that decreasing gas entropy also means shorter cooling time. Thus, if the  $K_0$  distribution is bimodal, the distribution of cooling times might also be bimodal. We have calculated cooling time profiles from the spectral analysis using the relation

$$t_{\text{cool}} = \frac{3nkT}{2n_e n_H \Lambda(T, Z)} \quad (5)$$

where  $t_{\text{cool}}$  is in seconds,  $n$  is the total ion number ( $\approx 2.3n_H$  for a fully ionized plasma),  $n_e$  and  $n_H$  are the electron and proton densities respectively,  $\Lambda(T, Z)$  is the cooling function for a given temperature and metal abundance, and  $3/2$  is a constant associated with isochoric cooling. The values of the cooling function,  $\Lambda(T, Z)$ , were calculated for each bin of a temperature profile with XSPEC using the flux of the best-fit spectral model. Following the procedure discussed in §3.4,  $\Lambda$

and  $kT$  were interpolated across the radial grid of the electron density profile. The cooling time profiles were then fit with a model analogous to that used for fitting  $K(r)$ :

$$t_{\text{cool}}(r) = t_0 + t_{100} \left( \frac{r}{100 \text{ kpc}} \right)^\alpha. \quad (6)$$

Shown in Figure 7 is the logarithmically binned and cumulative distributions of core cooling times.

As can be seen in Fig. 7, the distinct bimodality found in  $K_0$  is also present in cooling time. The KMM test for bimodality finds peaks at  $t_{c1} = 0.58 \pm 0.23 \text{ Gyr}$  and  $t_{c2} = 6.05 \pm 2.12 \text{ Gyr}$  with 128 and 94 in each population. The probability that the unimodal distribution is a better fit is once again exceedingly small,  $p = 1.59 \times 10^{-6}$ . The gap in  $t_0$  occurs at  $t_0 \approx 1 - 2 \text{ Gyrs}$ . The pile-up of core cooling times below 1 Gyr has been noted many times before, for example by Hu et al. (1985) and more recently by Dunn & Fabian (2008). This demonstrates that our cooling times are consistent with the results of others.

However, the  $K_0$  distribution can also be used to explore the distribution of core cooling times. Assuming free-free interactions are the dominant gas cooling mechanism (*i.e.*  $\epsilon \propto T^{1/2}$ ), Donahue et al. (2005) show that entropy is related to cooling time via the formulation:

$$t_{\text{cool}} \approx 10^8 \text{ yrs} \left( \frac{K}{10 \text{ keV cm}^2} \right)^{3/2} \left( \frac{kT}{5 \text{ keV}} \right)^{-1}. \quad (7)$$

Using this relationship to calculate core cooling time from entropy, we find the gap in cooling time occurs at  $t_{\text{cool}} \approx 0.7 - 1.0 \text{ Gyrs}$ . That the gaps in cooling time calculated from spectra and  $K_0$  are offset from each other suggests that while bimodality occurs only below a particular cooling time scale ( $\sim 1 \text{ Gyr}$ ), this may not be enough. The fundamental explanation of what is happening in cluster cores may be more closely coupled to gas entropy than gas cooling time. It is also interesting that the bimodality in  $K_0$  is sharper and deeper than it is in  $t_0$ .

Since cooling time profiles are more sensitive to the resolution of the temperature profiles than are the entropy profiles, it may be that resolution effects (*e.g.* our temperature interpolation scheme is too coarse, or averaging over many small-scale temperature fluctuations significantly increases  $t_0$ ) are limiting the quantification of the true cooling time of the core and hence altering  $t_0$ . But again, if entropy is more closely related to the physical processes in the cluster core than cooling time, then that the cooling time distribution does not present with the sharp, deep bimodality seen in  $K_0$  suggests entropy is the fundamental quantity related to bimodality.

#### 5.5. Slope and Normalization of Power-law Components

Beyond  $r \approx 100 \text{ kpc}$  the entropy profiles show a striking similarity in the slope of the power-law component which is independent of the core entropy value. For the full sample, the mean value of  $\alpha = 1.21 \pm 0.39$  while for clusters with  $K_0 < 50 \text{ keV cm}^2$ , mean  $\alpha = 1.19 \pm 0.38$ , and for clusters with  $K_0 \geq 50 \text{ keV cm}^2$ , mean  $\alpha = 1.23 \pm 0.40$ . The scaling factor of the power-law component,  $K_{100} \dots$  **[Discuss minimization of  $\chi^2$ ]** For the full sample, the mean value of  $K_{100} = 127 \pm 45 \text{ keV cm}^2$ . Again distinguishing between clusters below and above  $K_0 = 50 \text{ keV cm}^2$ , we find  $K_{100} = 151 \pm 50 \text{ keV cm}^2$  and  $K_{100} = 108 \pm 39 \text{ keV cm}^2$ , respectively. Scaling the entropy profiles by the cluster virial temperature and virial radius does reduce the dispersion of  $\alpha$  and scatter of  $K_{100}$ , but we reserve detailed discussion of scaling relations

for a future paper. This mean slope of  $\alpha \approx 1.2$ , is not statistically different from the theoretical value of 1.1 found by Tozzi & Norman (2001) in hierarchical cluster formation.

## 6. SUMMARY AND CONCLUSIONS

We have presented a sample of galaxy cluster entropy profiles created using archival *Chandra* data for 222 clusters (9.58 Msec), a project which we have named the Archive of Chandra Cluster Entropy Profile Tables, or *ACCEPT*. Our data reduction/analysis code (written in PERL and IDL), reduced data products, data tables, figures/plots, cluster images, and results of our analysis for all the clusters and observations are freely available at the *ACCEPT* web page<sup>7</sup>. We encourage observers and theorists to utilize this library of entropy profiles in their own work.

We created temperature profiles using spectra extracted from a minimum of three concentric annuli containing 2500 counts each and extending to either the chip edge or  $0.5R_{180}$ , whichever was smaller. We deprojected surface brightness profiles extracted from  $5''$  bins to obtain the electron gas density as a function of radius. Entropy profiles were then calculated from gas density and temperature using  $K(r) = T(r)n(r)^{-2/3}$ . Two models for the entropy distribution were then fit to each profile: a power-law only model and a power-law which approaches a constant value at small radii.

We have demonstrated that the entropy profiles for the vast majority of *ACCEPT* clusters are best fit by the model which approaches a constant entropy,  $K_0$ , in the core. The distribution of  $K_0$  for the full sample is also bimodal with the two populations separated by a poorly populated gap at  $K_0 \approx 40 - 60 \text{ keV cm}^2$ . For clusters approximately below and above this gap we find mean  $K_0 = 16.0 \pm 5.7 \text{ keV cm}^2$  and  $K_0 = 154 \pm 53 \text{ keV cm}^2$ , respectively. We also find bimodality in the primary *HIFLUGCS* subsample with the  $K_0$  gap and two populations having values consistent with the full *ACCEPT* sample. This indicates bimodality is not a result of archival bias. All of the entropy profiles in *ACCEPT* are remarkably similar at radii greater than 100 kpc, and asymptotically approach the self-similar pure-cooling curve ( $r \propto 1.1$ ) with a slope of  $\alpha = 1.21 \pm 0.39$ .

Two sets of cooling times were calculated for each cluster: 1) by using the results of the spectroscopic analysis, and 2) from converting  $K_0$  into a cooling time. The distribution of cooling times exhibits the same bimodality found in the  $K_0$  distribution. After comparing the cooling times from method (1) and (2), we find that the gap in the bimodal cooling time distributions occur at significantly different timescales:  $t_{\text{gap}} = 2 - 3 \text{ Gyrs}$  for the spectroscopic cooling times and  $t_{\text{gap}} = 0.7 - 1 \text{ Gyrs}$  for the cooling times determined using  $K_0$ .

<sup>7</sup> <http://www.pa.msu.edu/astro/MC2/accept>

After analyzing an ensemble of artificially redshifted entropy profiles, we find the lack of  $K_0 \lesssim 10 \text{ keV cm}^2$  clusters at  $z > 0.1$  is most likely a result of resolution effects. Investigation of possible systematics affecting best-fit  $K_0$  values, such as profile curvature and number of profile bins, revealed no trends which would significantly effect our results. We come to the conclusion that, indeed,  $K_0$  is a measure of average core entropy and not profile shape or resolution.

Voit & Donahue (2005) put forth a model of AGN feedback which explains observation of non-zero core entropy for the range  $K_0 \lesssim 70 \text{ keV cm}^2$ . In addition, the results of this project have already been used to reveal the existence of a core entropy threshold only below which  $H\alpha$  and powerful radio emission ( $\nu L_\nu > 10^{40} \text{ ergs s}^{-1}$ ) are predominantly found (Cavagnolo et al. 2008a). Voit et al. (2008) have suggested this entropy threshold is set by the process of electron thermal conduction in the cluster core. If merger events are capable of producing cluster cores with  $K_0 > 70 \text{ keV cm}^2$ , then taking these processes together – AGN feedback, conduction, and mergers – a closed-loop picture of the ICM’s entropy life-cycle is starting to emerge.

There are still many open questions regarding the evolution of the ICM and formation of thermal instabilities in cluster cores: How are clusters with  $K_0 > 100 \text{ keV cm}^2$  produced? What are the role of MHD instabilities, e.g. MTI (Balbus 2000; Quataert 2008) and HBI (Parrish & Quataert 2008), in shaping the ICM? Are the compact X-ray sources we find at the cores of some BCGs truly coronae? If so, how did they form and survive in the harsh ICM? We hope *ACCEPT* will be a useful resource in answering these questions.

K.W.C. thanks Chris Waters for supplying and supporting his new KMM bimodality code. K.W.C. was supported in this work through *Chandra* X-ray Observatory Archive grants AR-6016X and AR-4017A. M.D. acknowledges support from the NASA LTSA program NNG-05GD82G. The *Chandra* X-ray Observatory Center is operated by the Smithsonian Astrophysical Observatory for and on behalf of NASA under contract NAS8-03060. This research has made use of software provided by the Chandra X-ray Center in the application packages CIAO, CHIPS, and SHERPA. This research has made use of the NASA/IPAC Extragalactic Database which is operated by the Jet Propulsion Laboratory, California Institute of Technology, under contract with NASA. This research has also made use of NASA’s Astrophysics Data System. Some software was obtained from the High Energy Astrophysics Science Archive Research Center, provided by NASA’s Goddard Space Flight Center.

## REFERENCES

- Anders, E., & Grevesse, N. 1989, *Geochim. Cosmochim. Acta*, 53, 197  
 Arnaud, K. A. 1996, in *ASP Conf. Ser. 101: Astronomical Data Analysis Software and Systems V*, ed. G. H. Jacoby & J. Barnes, 17–+  
 Ashman, K. M., Bird, C. M., & Zepf, S. E. 1994, *AJ*, 108, 2348  
 Balbus, S. A. 2000, *ApJ*, 534, 420  
 Böhringer, H., Schuecker, P., Guzzo, L., Collins, C. A., Voges, W., Cruddace, R. G., Ortiz-Gil, A., Chincarini, G., De Grandi, S., Edge, A. C., MacGillivray, H. T., Neumann, D. M., Schindler, S., & Shaver, P. 2004, *A&A*, 425, 367  
 Bower, R. G., Benson, A. J., Malbon, R., Helly, J. C., Frenk, C. S., Baugh, C. M., Cole, S., & Lacey, C. G. 2006, *MNRAS*, 370, 645  
 Buote, D. A., & Tsai, J. C. 1996, *ApJ*, 458, 27  
 Burns, J. O., Roettiger, K., Pinkney, J., Perley, R. A., Owen, F. N., & Voges, W. 1995, *ApJ*, 446, 583  
 Cavagnolo, K. W., Donahue, M., Sun, M., & Voit, G. M. 2008a, *ArXiv e-prints*, arxiv:0806.0382  
 Cavagnolo, K. W., Donahue, M., Voit, G. M., & Sun, M. 2008b, *ArXiv e-prints*, arxiv:0803.3858  
 Cavaliere, A., & Fusco-Femiano, R. 1978, *A&A*, 70, 677  
 Chen, Y., Reiprich, T. H., Böhringer, H., Ikebe, Y., & Zhang, Y.-Y. 2007, *A&A*, 466, 805  
 Cowie, L. L., Songaila, A., Hu, E. M., & Cohen, J. G. 1996, *AJ*, 112, 839

- Croton, D. J., Springel, V., White, S. D. M., De Lucia, G., Frenk, C. S., Gao, L., Jenkins, A., Kauffmann, G., Navarro, J. F., & Yoshida, N. 2006, *MNRAS*, 365, 11
- David, L. P., Nulsen, P. E. J., McNamara, B. R., Forman, W., Jones, C., Ponman, T., Robertson, B., & Wise, M. 2001, *ApJ*, 557, 546
- Dickey, J. M., & Lockman, F. J. 1990, *ARA&A*, 28, 215
- Donahue, M., Horner, D. J., Cavagnolo, K. W., & Voit, G. M. 2006, *ApJ*, 643, 730
- Donahue, M., Voit, G. M., O'Dea, C. P., Baum, S. A., & Sparks, W. B. 2005, *ApJ*, 630, L13
- Dunn, R. J. H., & Fabian, A. C. 2008, *MNRAS*, 385, 757
- Ebeling, H., Edge, A. C., Allen, S. W., Crawford, C. S., Fabian, A. C., & Huchra, J. P. 2000, *MNRAS*, 318, 333
- Ebeling, H., Edge, A. C., Bohringer, H., Allen, S. W., Crawford, C. S., Fabian, A. C., Voges, W., & Huchra, J. P. 1998, *MNRAS*, 301, 881
- Ebeling, H., Edge, A. C., & Henry, J. P. 2001, *ApJ*, 553, 668
- Edge, A. C., & Stewart, G. C. 1991, *MNRAS*, 252, 414
- Edge, A. C., Stewart, G. C., Fabian, A. C., & Arnaud, K. A. 1990, *MNRAS*, 245, 559
- Ettori, S. 2000, *MNRAS*, 311, 313
- Evrard, A. E. 1997, *MNRAS*, 292, 289
- Evrard, A. E., Metzler, C. A., & Navarro, J. F. 1996, *ApJ*, 469, 494
- Fabian, A. C. 1994, *ARA&A*, 32, 277
- Feretti, L., Bohringer, H., Giovannini, G., & Neumann, D. 1997a, *A&A*, 317, 432
- Feretti, L., Giovannini, G., & Bohringer, H. 1997b, *New Astronomy*, 2, 501
- Finoguenov, A., Reiprich, T. H., & Böhringer, H. 2001, *A&A*, 368, 749
- Gioia, I. M., Maccacaro, T., Schild, R. E., Wolter, A., Stocke, J. T., Morris, S. L., & Henry, J. P. 1990, *ApJS*, 72, 567
- Guo, F., Oh, S. P., & Ruszkowski, M. 2008, *ArXiv e-prints*, arxiv:0804.3823
- Hallman, E. J., Burns, J. O., Motl, P. M., & Norman, M. L. 2007, *ApJ*, 665, 911
- Heckman, T. M., Baum, S. A., van Breugel, W. J. M., & McCarthy, P. 1989, *ApJ*, 338, 48
- Henry, J. P., Mullis, C. R., Voges, W., Böhringer, H., Briel, U. G., Gioia, I. M., & Huchra, J. P. 2006, *ApJS*, 162, 304
- Horner, D. J., Mushotzky, R. F., & Scharf, C. A. 1999, *ApJ*, 520, 78
- Hu, E. M., Cowie, L. L., & Wang, Z. 1985, *ApJS*, 59, 447
- Hudson, D. S., & Reiprich, T. H. 2007, in *Heating versus Cooling in Galaxies and Clusters of Galaxies*, ed. H. Böhringer, G. W. Pratt, A. Finoguenov, & P. Schuecker, 42–+
- Hudson, D. S., Reiprich, T. H., Clarke, T. E., & Sarazin, C. L. 2006, *A&A*, 453, 433
- Jeltema, T. E., Canizares, C. R., Bautz, M. W., & Buote, D. A. 2005, *ApJ*, 624, 606
- Kaiser, C. R., & Binney, J. 2003, *MNRAS*, 338, 837
- Kaiser, N. 1986, *MNRAS*, 222, 323
- Kalberla, P. M. W., Burton, W. B., Hartmann, D., Arnal, E. M., Bajaja, E., Morras, R., & Pöppel, W. G. L. 2005, *A&A*, 440, 775
- Kravtsov, A. V., Vikhlinin, A., & Nagai, D. 2006, *ApJ*, 650, 128
- Kriss, G. A., Cioffi, D. F., & Canizares, C. R. 1983, *ApJ*, 272, 439
- Lloyd-Davies, E. J., Ponman, T. J., & Cannon, D. B. 2000, *MNRAS*, 315, 689
- Loken, C., Norman, M. L., Nelson, E., Burns, J., Bryan, G. L., & Motl, P. 2002, *ApJ*, 579, 571
- Madau, P., Ferguson, H. C., Dickinson, M. E., Giavalisco, M., Steidel, C. C., & Fruchter, A. 1996, *MNRAS*, 283, 1388
- Maughan, B. J., Jones, C., Jones, L. R., & Van Speybroeck, L. 2007, *ApJ*, 659, 1125
- McCarthy, I. G., Babul, A., Bower, R. G., & Balogh, M. L. 2008, *MNRAS*, 386, 1309
- McNamara, B. R., & Nulsen, P. E. J. 2007, *ARA&A*, 45, 117
- McNamara, B. R., O'Connell, R. W., & Bregman, J. N. 1990, *ApJ*, 360, 20
- Mewe, R., Gronenschild, E. H. B. M., & van den Oord, G. H. J. 1985, *A&AS*, 62, 197
- Mewe, R., Lemen, J. R., & van den Oord, G. H. J. 1986, *A&AS*, 65, 511
- Mohr, J. J., Mathiesen, B., & Evrard, A. E. 1999, *ApJ*, 517, 627
- Molendi, S., de Grandi, S., Fusco-Femiano, R., Colafrancesco, S., Fiore, F., Nesci, R., & Tamburelli, F. 1999, *ApJ*, 525, L73
- Morandi, A., & Ettori, S. 2007, *MNRAS*, 380, 1521
- Nagai, D., Kravtsov, A. V., & Vikhlinin, A. 2007, *ApJ*, 668, 1
- Nevalainen, J., Markevitch, M., & Forman, W. 2000, *ApJ*, 536, 73
- O'Dea, C. P., Baum, S. A., Maloney, P. R., Tacconi, L. J., & Sparks, W. B. 1994, *ApJ*, 422, 467
- O'Hara, T. B., Mohr, J. J., & Guerrero, M. A. 2004, *ApJ*, 604, 604
- Parrish, I. J., & Quataert, E. 2008, *ApJ*, 677, L9
- Peres, C. B., Fabian, A. C., Edge, A. C., Allen, S. W., Johnstone, R. M., & White, D. A. 1998, *MNRAS*, 298, 416
- Peterson, J. R., Kahn, S. M., Paerels, F. B. S., Kaastra, J. S., Tamura, T., Bleeker, J. A. M., Ferrigno, C., & Jernigan, J. G. 2003, *ApJ*, 590, 207
- Peterson, J. R., Paerels, F. B. S., Kaastra, J. S., Arnaud, M., Reiprich, T. H., Fabian, A. C., Mushotzky, R. F., Jernigan, J. G., & Sakelliou, I. 2001, *A&A*, 365, L104
- Piffaretti, R., Jetzer, P., Kaastra, J. S., & Tamura, T. 2005, *A&A*, 433, 101
- Quataert, E. 2008, *ApJ*, 673, 758
- Rafferty, D., McNamara, B., & Nulsen, P. 2008, *ArXiv e-prints*, 802
- Reiprich, T. H. 2001, PhD thesis, AA(Max-Planck-Institut für extraterrestrische Physik, P.O. Box 1312, 85741 Garching, Germany)
- Reiprich, T. H., & Böhringer, H. 2002, *ApJ*, 567, 716
- Rosati, P., della Ceca, R., Burg, R., Norman, C., & Giacconi, R. 1995, *ApJ*, 445, L11
- Saro, A., Borgani, S., Tornatore, L., Dolag, K., Murante, G., Biviano, A., Calura, F., & Charlot, S. 2006, *MNRAS*, 373, 397
- Sharma, M., McNamara, B. R., Nulsen, P. E. J., Owers, M., Wise, M. W., Blanton, E. L., Sarazin, C. L., Owen, F. N., & David, L. P. 2004, *ApJ*, 613, 180
- Shaver, P. A., Wall, J. V., Kellermann, K. I., Jackson, C. A., & Hawkins, M. R. S. 1996, *Nature*, 384, 439
- Sun, M., Jones, C., Forman, W., Vikhlinin, A., Donahue, M., & Voit, M. 2007, *ApJ*, 657, 197
- Sun, M., Voit, G. M., Donahue, M., Jones, C., & Forman, W. 2008, *ArXiv e-prints*, arxiv:0805.2320
- Tamura, T., Kaastra, J. S., Peterson, J. R., Paerels, F. B. S., Mittaz, J. P. D., Trudolyubov, S. P., Stewart, G., Fabian, A. C., Mushotzky, R. F., Lumb, D. H., & Ikebe, Y. 2001, *A&A*, 365, L87
- Tozzi, P., & Norman, C. 2001, *ApJ*, 546, 63
- Ventimiglia, D., Voit, G. M., Borgani, S., & Donahue, M. 2008, *ApJ* Submitted
- Vikhlinin, A., Markevitch, M., Murray, S. S., Jones, C., Forman, W., & Van Speybroeck, L. 2005, *ApJ*, 628, 655
- Vikhlinin, A., McNamara, B. R., Forman, W., Jones, C., Quintana, H., & Hornstrup, A. 1998, *ApJ*, 502, 558
- Voit, G. M., Cavagnolo, K. W., Donahue, M., Rafferty, D. A., McNamara, B. R., & Nulsen, P. E. J. 2008, *ArXiv e-prints*, arxiv:0806.0384
- Voit, G. M., & Donahue, M. 1995, *ApJ*, 452, 164
- . 2005, *ApJ*, 634, 955
- Voit, G. M., Kay, S. T., & Bryan, G. L. 2005, *MNRAS*, 364, 909
- Wang, Q. D., Connolly, A., & Brunner, R. 1997, *ApJ*, 487, L13+
- Wang, Q. D., Owen, F., & Ledlow, M. 2004, *ApJ*, 611, 821
- Xue, Y.-J., & Wu, X.-P. 2000, *MNRAS*, 318, 715

## APPENDIX

NOTES ON CLUSTERS REQUIRING  $\beta$ -MODEL FIT

**NB:** In this section we abbreviate surface brightness as SB.

**Abell 119** ( $z = 0.0442$ ): This is a highly diffuse cluster without a prominent cool core. The large core region and slowly varying SB made deprojection highly unstable. We have excluded a small source at the very center of the BCG. The exclusion region for the source is  $\approx 2.2''$  in radius which at the redshift of the cluster is  $\sim 2$  kpc. This cluster required a double  $\beta$ -model.

**Abell 160** ( $z = 0.0447$ ): The highly asymmetric, low SB of this cluster resulted in a noisy surface brightness profile that could not be deprojected. This cluster required a double  $\beta$ -model. The BCG hosts a compact X-ray source. The exclusion region for the compact source has a radius of  $\sim 5''$  or  $\sim 4.3$  kpc. The BCG for this cluster is not coincident with the X-ray centroid and hence is not at the zero-point of our radial analysis.

**Abell 193** ( $z = 0.0485$ ): This cluster has an azimuthally symmetric and a very diffuse ICM centered on a BCG which is interacting with a companion galaxy. In Fig. 1 one can see that the central three bins of this cluster's SB profile are highly

discrepant from the best-fit  $\beta$ -model. This is a result of the BCG being coincident with a bright, compact X-ray source. As we have concluded in 3.5, compact X-ray sources are excluded from our analysis as they are not the focus of our study here. Hence we have used the best-fit  $\beta$ -model in deriving  $K(r)$  instead of the raw SB.

**Abell 400** ( $z = 0.0240$ ): The two ellipticals at the center of this cluster have compact X-ray sources which are excluded during analysis. The core entropy we derive for this cluster is in agreement with that found by Hudson et al. (2006) which supports the accuracy of the  $\beta$ -model we have used.

**Abell 1240** ( $z = 0.1590$ ): The SB of this cluster is well-modeled by a  $\beta$ -model. There is nothing peculiar worth noting about the BCG or the core of this cluster.

**Abell 1736** ( $z = 0.0338$ ): Another “boring” cluster with a very diffuse low SB ICM, no peaky core, and no signs of merger activity in the X-ray. The noisy SB profile necessitated the use of a double  $\beta$ -model. The BCG is coincident with a very compact X-ray source, but the BCG is offset from the X-ray centroid and thus the central bins are not adversely affected. The radius of the exclusion region for the compact source is  $\approx 2.3''$  or 1.5 kpc.

**Abell 2125** ( $z = 0.2465$ ): Although the ICM of this cluster is very similar to the other clusters listed here (*i.e.* diffuse, large cores), A2125 is one of the more compact clusters. The presence of several merging sub-clusters (Wang et al. 1997, 2004) to the NW of the main cluster form a diffuse mass which cannot rightly be excluded. This complication yields inversions of the deprojected SB profile if a double  $\beta$ -model is not used.

**Abell 2255** ( $z = 0.0805$ ): This is a very well studied merger cluster (Burns et al. 1995; Feretti et al. 1997a). The core of this cluster is very large ( $r > 200$  kpc). Such large extended cores cannot be deprojected using our methods because if too many neighboring bins have approximately the same SB, deprojection results in bins with negative or zero value. The SB for this cluster is well modeled as a  $\beta$  function.

**Abell 2319** ( $z = 0.0562$ ): A2319 is another well studied merger cluster (Feretti et al. 1997b; Molendi et al. 1999) with a very large core region ( $r > 100$  kpc) and a prominent cold front (O’Hara et al. 2004). Once again, the SB profile is well-fit by a  $\beta$ -model.

**Abell 2462** ( $z = 0.0737$ ): This cluster is very similar in appearance to A193: highly symmetric ICM with a bright, compact X-ray source embedded at the center of an extended diffuse ICM. The central compact source has been excluded from our analysis with a region of radius  $\approx 1.5''$  or  $\sim 3$  kpc. The central bin of the SB profile is most likely boosted above the best-fit double  $\beta$ -model because of faint extended emission from the compact source which cannot be discerned from the ambient ICM.

**Abell 2631** ( $z = 0.2779$ ): The SB profile for this cluster is rather regular, but because the cluster has a large core it suffers from the same unstable deprojection as A2255 and A2319. The ICM is symmetric about the BCG and is incredibly uniform in the core region. We did not detect or exclude a source at the center of this cluster, but under heavy binning the cluster image appears to have a source coincident with the BCG, and the slightly higher flux in central bin of the SB profile may be a result of an unresolved source.

**Abell 3376** ( $z = 0.0456$ ): The large core of this cluster ( $r > 120$  kpc) makes deprojection unstable and a  $\beta$ -model must be used.

**Abell 3391** ( $z = 0.0560$ ): The BCG is coincident with a compact X-ray source. The source is excluded using a region with radius  $\approx 2''$  or  $\sim 2$  kpc. The large uniform core region made deprojection unstable and thus required a  $\beta$ -model fit.

**Abell 3395** ( $z = 0.0510$ ): The SB profile for this cluster is noisy resulting in deprojection inversions and requiring a  $\beta$ -model fit. The BCG of this cluster has a compact X-ray source and this source was excluded using a region with radius  $\approx 1.9''$  or  $\sim 2$  kpc.

**MKW 08** ( $z = 0.0270$ ): MKW 08 is a nearby large group/poor cluster with a pair of interacting elliptical galaxies in the core. The BCG falls directly in the middle of the ACIS-I detector gap. However, despite the lack of proper exposure, CCD dithering reveals that a very bright X-ray source is associated with the BCG. A double  $\beta$ -model was necessary for this cluster because the low SB of the ICM is noisy and deprojection is unstable.

**RBS 461** ( $z = 0.0290$ ): This is another nearby large group/poor cluster with an extended, diffuse, axisymmetric, featureless ICM centered on the BCG. The BCG is coincident with a compact source with size  $r \approx 1.7$  kpc. This source was excluded during reduction. The  $\beta$ -model is a good fit to the SB profile.

TABLE 1  
SUMMARY OF SAMPLE

Cluster – (1)	Obs. ID – (2)	R.A. hr:min:sec (3)	Decl. ° : ' : '' (4)	Exp. Time ksec (5)	Mode – (6)	ACIS – (7)	z – (8)	$kT_X$ keV (9)	$K_0$ keV cm <sup>2</sup> (10)	$L_{bol}$ 10 <sup>44</sup> ergs s <sup>-1</sup> (11)	Notes – (12)
1E0657 56	3184	06:58:29.627	-55:56:39.79	87.5	VF	I3	0.2960	11.64	307.4 ± 19.3	52.50	–
–	5356	–	–	97.2	VF	I2	–	–	–	–	–
–	5361	–	–	82.6	VF	I3	–	–	–	–	–
2A 335+096	919	03:38:41.105	+09:58:00.66	19.7	F	S3	0.0347	2.88	7.1 ± 0.1	9.77	–
2PIGG J0011.5-2850	5797	00:11:21.623	-28:51:14.44	19.9	VF	I3	0.0753	5.15	102.0 ± 42.9	2.17	–
2PIGG J2227.0-3041	5798	22:27:54.560	-30:34:34.84	22.3	VF	I2	0.0729	2.79	17.1 ± 1.0	0.81	–
3C 28.0	3233	00:55:50.401	+26:24:36.47	49.7	VF	I3	0.1952	5.53	23.9 ± 1.3	4.83	–
3C 295	2254	14:11:20.280	+52:12:10.55	90.9	VF	I3	0.4641	5.16	14.5 ± 2.5	7.01	d
3C 388	5295	18:44:02.365	+45:33:29.31	30.7	VF	I3	0.0917	3.23	17.0 ± 5.8	0.53	d
4C 55.16	4940	08:34:54.923	+55:34:21.15	96.0	VF	S3	0.2420	4.98	23.3 ± 2.9	5.97	d
Abell 13	4945	00:13:37.883	-19:30:09.10	55.3	VF	S3	0.0940	6.84	182.6 ± 26.2	1.42	–
Abell 68	3250	00:37:06.475	+09:09:32.28	10.0	VF	I3	0.2546	9.01	217.3 ± 89.0	12.80	–
Abell 85	904	00:41:50.406	-09:18:10.79	38.4	F	I0	0.0558	6.40	12.5 ± 0.5	5.30	–
Abell 119	4180	00:56:15.150	-01:14:59.70	11.9	VF	I3	0.0442	5.86	233.8 ± 87.7	1.41	a,e
Abell 133	2203	01:02:41.756	-21:52:49.79	35.5	F	S3	0.0558	4.31	17.3 ± 0.5	0.83	–
Abell 160	3219	01:13:00.692	+15:29:15.08	58.5	VF	I3	0.0447	2.70	155.8 ± 27.7	-0.00	a,e
Abell 193	6931	01:25:07.660	+08:41:57.08	17.9	VF	S3	0.0485	2.50	188.9 ± 7.9	-0.00	a,e
Abell 209	3579	01:31:52.565	-13:36:38.79	10.0	VF	I3	0.2060	8.28	105.5 ± 26.9	11.00	–
–	522	–	–	10.0	VF	I3	–	–	–	–	–
Abell 222	4967	01:37:34.562	-12:59:34.88	45.1	VF	I3	0.2130	4.60	126.0 ± 15.0	10.50	–
Abell 223	49671	01:37:55.963	-12:49:10.53	45.1	VF	I0	0.2070	5.28	183.9 ± 46.1	11.20	e
Abell 262	2215	01:52:46.299	+36:09:11.80	28.7	VF	S3	0.0164	2.18	10.6 ± 0.8	1.05	–
–	7921	–	–	110.7	VF	S3	–	–	–	–	–
Abell 267	1448	01:52:42.269	+01:00:45.33	7.9	F	I3	0.2300	6.79	168.6 ± 17.6	8.62	–
–	3580	–	–	19.9	VF	I3	–	–	–	–	–
Abell 368	9412	02:37:27.640	-26:30:28.99	18.4	VF	I3	0.2200	5.62	50.9 ± 8.2	-0.00	–
Abell 370	515	02:39:53.169	-01:34:36.96	88.0	F	S3	0.3747	7.35	367.6 ± 58.9	12.10	–
Abell 383	2321	02:48:03.364	-03:31:44.69	19.5	F	S3	0.1871	4.91	13.0 ± 1.6	5.39	–
Abell 399	3230	02:57:53.382	+13:01:30.86	48.6	VF	I0	0.0716	7.95	153.2 ± 18.8	4.40	–
Abell 400	4181	02:57:41.603	+06:01:27.61	21.5	VF	I3	0.0240	2.31	162.8 ± 3.9	0.85	a,e
Abell 401	2309	02:58:56.920	+13:34:14.51	11.6	F	I2	0.0745	8.07	166.9 ± 7.7	8.39	–
–	518	–	–	18.0	F	I3	–	–	–	–	–
Abell 426	3209	03:19:48.194	+41:30:40.73	95.8	F	S3	0.0179	3.55	19.4 ± 0.2	50.00	d
–	4289	–	–	95.4	F	S3	–	–	–	–	–
Abell 478	1669	04:13:25.345	+10:27:55.15	42.4	F	S3	0.0883	7.07	7.8 ± 0.9	16.40	–
–	6102	–	–	10.0	VF	I3	–	–	–	–	–
Abell 496	3361	04:33:38.038	-13:15:39.65	10.0	VF	S3	0.0328	5.03	8.9 ± 0.7	0.57	–
Abell 520	4215	04:54:10.303	+02:55:36.48	66.3	VF	I3	0.2020	9.29	325.5 ± 29.2	13.10	–
Abell 521	430	04:54:06.337	-10:13:16.88	39.1	VF	S3	0.2533	7.03	259.9 ± 36.2	9.85	–
Abell 539	5808	05:16:37.335	+06:26:25.18	24.3	VF	I3	0.0288	3.24	22.6 ± 4.5	1.82	b,e
–	7209	–	–	18.6	VF	I3	–	–	–	–	–
Abell 562	6936	06:53:21.524	+69:19:51.19	51.5	VF	S3	0.1100	3.04	202.1 ± 39.3	2.14	e
Abell 576	3289	07:21:30.394	+55:45:41.95	38.6	VF	S3	0.0385	4.43	95.3 ± 15.4	0.47	e
Abell 586	530	07:32:20.339	+31:37:58.59	10.0	VF	I3	0.1710	6.47	94.8 ± 19.2	8.61	–
Abell 611	3194	08:00:56.832	+36:03:24.09	36.1	VF	S3	0.2880	7.06	124.9 ± 18.6	10.90	e
Abell 644	2211	08:17:25.225	-07:30:40.03	29.7	VF	I3	0.0698	7.73	132.4 ± 9.2	7.61	–
Abell 665	3586	08:30:59.226	+65:50:20.06	29.7	VF	I3	0.1810	7.45	134.6 ± 23.4	13.50	–
Abell 697	4217	08:42:57.549	+36:21:57.65	19.5	VF	I3	0.2820	9.52	166.7 ± 24.4	26.30	–
Abell 744	6947	09:07:20.455	+16:39:06.18	39.5	VF	I3	0.0729	2.50	63.4 ± 10.2	0.89	e
Abell 754	577	09:09:18.188	-09:41:09.56	44.2	F	I3	0.0543	9.94	270.4 ± 23.8	33.10	–
Abell 773	5006	09:17:52.566	+51:43:38.18	19.8	VF	I3	0.2170	7.83	244.3 ± 31.7	13.00	–
Abell 907	3185	09:58:21.946	-11:03:50.73	48.0	VF	I3	0.1527	5.59	23.4 ± 3.2	6.25	–
–	3205	–	–	47.1	VF	I3	–	–	–	–	–
–	535	–	–	11.0	VF	I3	–	–	–	–	–
Abell 963	903	10:17:03.744	+39:02:49.17	36.3	F	S3	0.2056	6.73	55.8 ± 12.9	10.70	–
Abell 1063S	4966	22:48:44.294	-44:31:48.37	26.7	VF	I3	0.3540	11.96	169.6 ± 19.7	71.50	–
Abell 1068	1652	10:40:44.520	+39:57:10.28	26.8	F	S3	0.1375	4.62	9.1 ± 1.0	4.77	–
Abell 1201	4216	11:12:54.489	+13:26:08.76	39.7	VF	S3	0.1688	5.61	64.8 ± 16.9	4.08	–
Abell 1204	2205	11:13:20.419	+17:35:38.45	23.6	VF	I3	0.1706	3.63	15.3 ± 1.4	3.98	–
Abell 1240	4961	11:23:38.357	+43:05:48.33	51.3	VF	I3	0.1590	4.77	462.4 ± 41.7	-0.00	a
Abell 1361	2200	11:43:39.637	+46:21:20.41	16.7	F	S3	0.1171	5.32	18.6 ± 4.9	2.39	–
Abell 1413	5003	11:55:17.893	+23:24:21.84	75.1	VF	I2	0.1426	7.41	64.0 ± 8.3	10.20	–
Abell 1423	538	11:57:17.263	+33:36:37.44	9.8	VF	I3	0.2130	6.01	68.3 ± 12.8	7.07	–
Abell 1446	4975	12:02:03.744	+58:02:17.93	58.4	VF	S3	0.1035	4.00	152.4 ± 43.8	-0.00	–
Abell 1569	6100	12:36:26.015	+16:32:17.81	41.2	VF	I3	0.0735	2.51	110.1 ± 27.8	-0.00	–
Abell 1644	2206	12:57:11.665	-17:24:32.86	18.7	F	I3	0.0471	4.60	19.0 ± 1.2	-0.00	b
–	7922	–	–	51.5	VF	I3	–	–	–	–	–
Abell 1650	4178	12:58:41.499	-01:45:44.32	27.3	VF	S3	0.0843	6.17	38.0 ± 9.9	4.37	–
Abell 1651	4185	12:59:22.830	-04:11:45.86	9.6	VF	I3	0.0840	6.26	89.5 ± 11.1	6.71	–
Abell 1664	1648	13:03:42.622	-24:14:41.59	9.8	VF	S3	0.1276	4.39	14.4 ± 1.0	3.14	–
–	7901	–	–	36.6	VF	S3	–	–	–	–	–
Abell 1689	1663	13:11:29.612	-01:20:28.69	10.7	F	I3	0.1843	10.10	78.4 ± 7.6	24.70	–
–	5004	–	–	19.9	VF	I3	–	–	–	–	–
–	540	–	–	10.3	F	I3	–	–	–	–	–

TABLE 1 — *Continued*

Cluster — (1)	Obs. ID — (2)	R.A. hr:min:sec (3)	Decl. ° : ' : '' (4)	Exp. Time ksec (5)	Mode — (6)	ACIS — (7)	z — (8)	$kT_X$ keV (9)	$K_0$ keV cm <sup>2</sup> (10)	$L_{bol}$ 10 <sup>44</sup> ergs s <sup>-1</sup> (11)	Notes — (12)
Abell 1736	4186	13:26:49.453	-27:09:48.13	14.9	VF	I1	0.0338	3.45	150.3 ± 38.2	3.47	a,e
Abell 1758	2213	13:32:48.398	+50:32:32.53	58.3	VF	S3	0.2792	12.14	230.8 ± 37.2	21.10	—
Abell 1763	3591	13:35:17.957	+40:59:55.80	19.6	VF	I3	0.1866	7.78	214.7 ± 32.8	9.33	—
Abell 1795	493	13:48:52.802	+26:35:23.55	19.6	VF	S3	0.0625	7.80	19.0 ± 1.1	7.59	—
—	5289	—	—	15.0	VF	I3	—	—	—	—	—
Abell 1835	495	14:01:01.951	+02:52:43.18	19.5	F	S3	0.2532	9.77	11.4 ± 2.5	39.60	—
Abell 1914	3593	14:26:03.060	+37:49:27.84	18.9	VF	I3	0.1712	9.62	107.2 ± 18.0	26.40	—
Abell 1942	3290	14:38:21.878	+03:40:12.97	57.6	VF	I2	0.2240	4.77	107.7 ± 77.7	2.30	—
Abell 1991	3193	14:54:31.620	+18:38:41.48	38.3	VF	S3	0.0587	2.67	1.5 ± 0.3	0.45	—
Abell 1995	7021	14:52:57.410	+58:02:56.84	48.5	VF	I3	0.3186	3.40	374.4 ± 60.1	38.00	—
Abell 2029	4977	15:10:56.139	+05:44:40.47	77.9	F	S3	0.0765	7.38	10.5 ± 0.7	58.90	—
—	6101	—	—	9.9	VF	I3	—	—	—	—	—
—	891	—	—	19.8	F	S3	—	—	—	—	—
Abell 2034	2204	15:10:12.498	+33:30:39.57	53.9	VF	I3	0.1130	7.15	232.6 ± 23.0	6.50	—
Abell 2052	5807	15:16:44.514	+07:01:17.02	127.0	VF	S3	0.0353	2.98	9.4 ± 0.7	5.13	d
—	890	—	—	36.8	F	S3	—	—	—	—	—
Abell 2063	4187	15:23:04.851	+08:36:20.16	8.8	VF	I3	0.0351	3.61	53.5 ± 2.6	4.27	—
—	6263	—	—	16.8	VF	S3	—	—	—	—	—
Abell 2065	31821	15:22:29.517	+27:42:22.93	27.7	VF	I3	0.0730	5.75	44.0 ± 6.5	2.95	—
Abell 2069	4965	15:24:11.376	+29:52:19.02	55.4	VF	I2	0.1160	6.50	453.2 ± 35.6	3.85	—
Abell 2104	895	15:40:08.131	-03:18:15.02	49.2	F	S3	0.1554	8.53	160.6 ± 42.2	6.98	—
Abell 2107	4960	15:39:39.113	+21:46:57.66	35.6	VF	I3	0.0411	3.82	21.2 ± 5.8	3.02	b
Abell 2111	544	15:39:40.637	+34:25:28.01	10.3	F	I3	0.2300	7.13	107.4 ± 97.3	7.51	—
Abell 2124	3238	15:44:59.131	+36:06:34.11	19.4	VF	S3	0.0658	4.73	98.3 ± 23.9	0.46	—
Abell 2125	2207	15:41:14.154	+66:15:57.20	81.5	VF	I3	0.2465	2.88	225.2 ± 32.0	0.79	a
Abell 2142	1196	15:58:20.880	+27:13:44.21	11.4	F	S3	0.0898	8.24	68.1 ± 2.5	75.90	—
—	1228	—	—	12.1	F	S3	—	—	—	—	—
—	5005	—	—	44.6	VF	I3	—	—	—	—	—
Abell 2147	3211	16:02:17.025	+15:58:28.32	17.9	VF	I3	0.0356	4.09	151.9 ± 27.2	0.73	—
Abell 2151	4996	16:04:35.887	+17:43:17.36	21.8	VF	I3	0.0366	2.90	0.4 ± 3.6	1.41	e
Abell 2163	1653	16:15:45.705	-06:09:00.62	71.1	VF	I1	0.1695	19.20	438.0 ± 82.6	49.30	—
Abell 2199	497	16:28:38.249	+39:33:04.28	19.5	F	S3	0.0300	4.55	13.3 ± 0.8	0.81	b
Abell 2204	499	16:32:46.920	+05:34:32.86	10.1	F	S3	0.1524	6.97	9.7 ± 0.9	22.00	—
—	6104	—	—	9.6	VF	I3	—	—	—	—	—
—	7940	—	—	77.1	VF	I3	—	—	—	—	—
Abell 2218	1666	16:35:50.831	+66:12:42.31	48.6	VF	I0	0.1713	7.35	288.6 ± 20.0	8.46	—
Abell 2219	896	16:40:20.112	+46:42:42.84	42.3	F	S3	0.2256	12.75	411.6 ± 43.2	38.30	—
Abell 2244	4179	17:02:42.579	+34:03:37.34	57.0	VF	S3	0.0967	5.68	57.6 ± 4.2	5.54	—
Abell 2255	894	17:12:42.935	+64:04:10.81	39.4	F	I3	0.0805	6.12	529.1 ± 28.2	3.70	a
Abell 2259	3245	17:20:08.299	+27:40:11.53	10.0	VF	I3	0.1640	5.18	114.0 ± 18.9	5.43	—
Abell 2261	5007	17:22:27.254	+32:07:58.60	24.3	VF	I3	0.2240	7.63	61.1 ± 8.1	17.60	—
Abell 2294	3246	17:24:10.149	+85:53:09.77	10.0	VF	I3	0.1780	9.98	156.3 ± 52.7	10.40	—
Abell 2319	3231	19:21:09.638	+43:57:21.53	14.4	VF	I1	0.0562	10.87	270.2 ± 4.8	12.70	a
Abell 2384	4202	21:52:21.178	-19:32:51.90	31.5	VF	I3	0.0945	4.75	38.5 ± 3.0	1.98	—
Abell 2390	4193	21:53:36.825	+17:41:44.38	95.1	VF	S3	0.2301	11.15	14.7 ± 7.0	35.60	—
Abell 2409	3247	22:00:52.567	+20:58:06.55	10.2	VF	I3	0.1479	5.94	73.8 ± 20.7	7.08	—
Abell 2462	4159	22:39:11.367	-17:20:28.33	39.2	VF	S3	0.0737	2.50	129.7 ± 27.0	-0.00	a,e
Abell 2537	4962	23:08:22.313	-02:11:29.88	36.2	VF	S3	0.2950	8.40	110.4 ± 19.4	10.20	—
Abell 2554	1696	23:12:19.622	-21:30:11.32	19.9	VF	S3	0.1103	5.29	105.1 ± 71.8	1.66	—
Abell 2556	2226	23:13:01.413	-21:38:04.47	19.9	VF	S3	0.0862	3.50	12.4 ± 1.3	1.53	—
Abell 2589	3210	23:23:57.315	+16:46:38.43	13.7	VF	S3	0.0415	3.65	52.0 ± 39.2	0.33	—
Abell 2597	922	23:25:19.779	-12:07:27.63	39.4	F	S3	0.0854	4.02	10.6 ± 1.5	1.47	—
Abell 2626	3192	23:36:30.452	+21:08:47.36	24.8	VF	S3	0.0573	3.29	23.2 ± 2.9	0.66	—
Abell 2631	3248	23:37:38.560	+00:16:05.02	9.2	VF	I3	0.2779	7.06	308.8 ± 37.4	12.70	a
Abell 2657	4941	23:44:57.253	+09:11:30.74	16.1	VF	I3	0.0402	3.77	65.4 ± 12.0	4.27	—
Abell 2667	2214	23:51:39.395	-26:05:02.75	9.6	VF	S3	0.2300	6.75	19.3 ± 3.4	20.10	—
Abell 2717	6974	00:03:12.968	-35:56:00.13	19.8	VF	I3	0.0475	1.69	27.1 ± 8.4	0.26	e
Abell 2744	2212	00:14:19.529	-30:23:30.24	24.8	VF	S3	0.3080	9.18	438.4 ± 58.7	29.20	—
—	7915	—	—	18.6	VF	I3	—	—	—	—	—
—	8477	—	—	45.9	VF	I3	—	—	—	—	—
—	8557	—	—	27.8	VF	I3	—	—	—	—	—
Abell 2813	9409	00:43:24.881	-20:37:25.08	19.9	VF	I3	0.2924	8.39	267.6 ± 43.8	-0.00	—
Abell 3084	9413	03:04:03.920	-36:56:27.17	19.9	VF	I3	0.0977	4.56	96.7 ± 13.4	-0.00	—
Abell 3088	9414	03:07:01.734	-28:39:55.47	18.9	VF	I3	0.2534	6.71	82.8 ± 8.4	38.90	—
Abell 3112	2516	03:17:57.681	-44:14:17.16	16.9	VF	S3	0.0720	5.17	11.4 ± 1.4	3.28	d
Abell 3120	6951	03:21:56.464	-51:19:35.40	26.8	VF	I3	0.0690	4.39	17.3 ± 3.5	-0.00	—
Abell 3158	3201	03:42:54.675	-53:37:24.36	24.8	VF	I3	0.0580	4.94	166.0 ± 11.7	3.45	—
—	3712	—	—	30.9	VF	I3	—	—	—	—	—
Abell 3266	899	04:31:13.304	-61:27:12.59	29.8	VF	I1	0.0590	9.07	72.5 ± 49.7	2.77	—
Abell 3376	3202	06:02:11.756	-39:56:59.07	44.3	VF	I3	0.0456	4.08	282.9 ± 9.3	0.75	a
—	3450	—	—	19.8	VF	I3	—	—	—	—	—
Abell 3391	4943	06:26:21.511	-53:41:44.81	18.4	VF	I3	0.0560	6.07	367.5 ± 16.0	1.44	a,e
Abell 3395	4944	06:26:48.463	-54:32:59.21	21.9	VF	I3	0.0510	5.13	247.2 ± 25.2	5.75	a,e
Abell 3528S	8268	12:54:40.897	-29:13:38.10	8.1	VF	I3	0.0530	4.94	31.6 ± 2.3	-0.00	—
Abell 3558	1646	13:27:56.854	-31:29:43.78	14.4	VF	S3	0.0480	6.60	126.2 ± 11.8	1.62	e



TABLE 1 — *Continued*

Cluster — (1)	Obs. ID — (2)	R.A. hr:min:sec (3)	Decl. ° : ' : '' (4)	Exp. Time ksec (5)	Mode — (6)	ACIS — (7)	z — (8)	$kT_X$ keV (9)	$K_0$ keV cm <sup>2</sup> (10)	$L_{bol}$ 10 <sup>44</sup> ergs s <sup>-1</sup> (11)	Notes — (12)
Abell 3562	4167	13:33:37.800	-31:40:12.04	19.3	VF	I2	0.0490	4.59	77.4 ± 8.9	1.11	—
Abell 3571	4203	13:47:28.434	-32:51:52.45	34.0	VF	S3	0.0391	7.77	71.0 ± 9.3	1.25	—
Abell 3581	1650	14:07:29.777	-27:01:05.88	7.2	VF	S3	0.0218	2.10	9.5 ± 0.8	1.23	d
Abell 3667	5751	20:12:41.231	-56:50:35.70	128.9	VF	I3	0.0556	6.51	160.4 ± 15.5	4.25	—
—	5752	—	—	60.4	VF	I3	—	—	—	—	—
—	5753	—	—	103.6	VF	I3	—	—	—	—	—
—	889	—	—	50.3	F	I2	—	—	—	—	—
Abell 3822	8269	21:54:04.203	-57:52:02.71	8.1	VF	I3	0.0759	5.45	108.7 ± 76.4	-0.00	e
Abell 3921	4973	22:49:57.829	-64:25:42.17	29.4	VF	I3	0.0927	5.69	101.2 ± 17.9	3.37	—
Abell 4038	4992	23:47:43.180	-28:08:34.81	33.5	VF	I2	0.0300	3.11	37.9 ± 1.2	0.82	—
Abell 4059	5785	23:57:01.065	-34:45:33.28	92.1	VF	S3	0.0475	4.69	7.1 ± 1.1	6.76	—
Abell S0405	8272	03:51:32.815	-82:13:10.19	7.9	VF	I3	0.0613	4.63	16.9 ± 27.9	-0.00	—
Abell S0592	9420	06:38:48.610	-53:58:26.32	19.9	VF	I3	0.2216	8.24	58.7 ± 14.4	-0.00	—
AC 114	1562	22:58:48.316	-34:48:08.20	72.5	F	S3	0.3120	7.53	199.8 ± 28.0	11.00	—
AWM7	908	02:54:27.631	+41:34:47.07	47.9	F	I3	0.0172	3.71	8.4 ± 1.3	4.07	b
Centaurus	4190	12:48:49.267	-41:18:39.54	34.3	VF	S3	0.0109	3.96	2.2 ± 0.0	1.74	b
—	4191	—	—	34.0	VF	S3	—	—	—	—	—
—	4954	—	—	89.1	F	S3	—	—	—	—	—
—	4955	—	—	44.7	F	S3	—	—	—	—	—
—	504	—	—	31.8	F	S3	—	—	—	—	—
—	505	—	—	10.0	F	S3	—	—	—	—	—
—	5310	—	—	49.3	F	S3	—	—	—	—	—
CID 72	2018	17:33:03.247	+43:45:37.28	30.7	F	S3	0.0344	2.88	9.4 ± 0.3	-0.00	—
—	6949	—	—	38.6	VF	I3	—	—	—	—	—
—	7321	—	—	37.5	VF	I3	—	—	—	—	—
—	7322	—	—	37.5	VF	I3	—	—	—	—	—
CL J1226.9+3332	3180	12:26:58.373	+33:32:47.36	31.7	VF	I3	0.8900	10.00	166.0 ± 45.2	30.80	—
—	5014	—	—	32.7	VF	I3	—	—	—	—	—
—	932	—	—	9.8	VF	S3	—	—	—	—	—
Cygnus A	360	19:59:28.381	+40:44:01.98	34.7	F	S3	0.0561	7.68	23.6 ± 0.9	2.18	d
ESO 3060170	3188	05:40:06.687	-40:50:12.82	14.0	VF	I3	0.0358	2.79	8.0 ± 1.0	0.66	b
—	3189	—	—	14.1	VF	I0	—	—	—	—	—
ESO 5520200	3206	04:54:52.318	-18:06:56.52	23.9	VF	I3	0.0314	2.37	5.9 ± 4.2	0.09	—
EXO 422-086	4183	04:25:51.271	-08:33:36.42	10.0	VF	I3	0.0397	3.40	13.8 ± 0.8	0.74	—
HCG 62	921	12:53:05.741	-09:12:15.64	48.5	F	S3	0.0146	1.10	3.4 ± 0.1	0.08	—
HCG 42	3215	10:00:14.234	-19:38:10.77	31.7	VF	S3	0.0133	0.70	1.9 ± 0.3	0.02	—
Hercules A	1625	16:51:08.161	+04:59:32.44	14.8	VF	S3	0.1541	5.21	9.2 ± 1.3	3.48	—
—	5796	—	—	47.5	VF	S3	—	—	—	—	—
—	6257	—	—	49.5	VF	S3	—	—	—	—	—
Hydra A	4970	09:18:05.985	-12:05:43.94	98.8	VF	S3	0.0549	4.00	13.3 ± 0.7	2.63	d
—	576	—	—	19.5	F	S3	—	—	—	—	—
M49	321	12:29:46.841	+08:00:01.98	39.6	VF	S3	0.0033	1.33	0.9 ± 0.1	-0.00	c
M87	5826	12:30:49.383	+12:23:28.67	126.8	VF	I3	0.0044	2.50	3.5 ± 0.1	-0.00	d
—	5827	—	—	156.2	VF	I3	—	—	—	—	—
MACS J0011.7-1523	3261	00:11:42.965	-15:23:20.79	21.6	VF	I3	0.3600	5.42	18.8 ± 6.3	10.80	—
—	6105	—	—	37.3	VF	I3	—	—	—	—	—
MACS J0035.4-2015	3262	00:35:26.573	-20:15:46.06	21.4	VF	I3	0.3644	7.39	93.4 ± 15.7	19.80	—
MACS J0159.8-0849	3265	01:59:49.453	-08:50:00.90	17.9	VF	I3	0.4050	9.59	18.8 ± 3.8	26.30	—
—	6106	—	—	35.3	VF	I3	—	—	—	—	—
MACS J0242.5-2132	3266	02:42:35.906	-21:32:26.30	11.9	VF	I3	0.3140	5.58	10.9 ± 1.9	12.90	—
MACS J0257.1-2325	1654	02:57:09.130	-23:26:05.85	19.8	F	I3	0.5053	10.50	234.5 ± 68.2	21.70	—
—	3581	—	—	18.5	VF	I3	—	—	—	—	—
MACS J0257.6-2209	3267	02:57:41.024	-22:09:11.12	20.5	VF	I3	0.3224	8.02	155.9 ± 25.0	10.90	—
MACS J0308.9+2645	3268	03:08:55.927	+26:45:38.34	24.4	VF	I3	0.3240	10.54	212.8 ± 53.9	20.60	—
MACS J0329.6-0211	3257	03:29:41.681	-02:11:47.67	9.9	VF	I3	0.4500	5.20	11.1 ± 2.5	12.80	—
—	3582	—	—	19.9	VF	I3	—	—	—	—	—
—	6108	—	—	39.6	VF	I3	—	—	—	—	—
MACS J0417.5-1154	3270	04:17:34.686	-11:54:32.71	12.0	VF	I3	0.4400	11.07	27.1 ± 7.3	38.20	—
MACS J0429.6-0253	3271	04:29:36.088	-02:53:09.02	23.2	VF	I3	0.3990	5.66	17.2 ± 4.3	11.70	—
MACS J0520.7-1328	3272	05:20:42.052	-13:28:49.38	19.2	VF	I3	0.3398	6.27	88.6 ± 22.0	9.63	—
MACS J0547.0-3904	3273	05:47:01.582	-39:04:28.24	21.7	VF	I3	0.2100	3.58	23.1 ± 4.4	1.62	e
MACS J0717.5+3745	1655	07:17:31.654	+37:45:18.52	19.9	F	I3	0.5480	10.50	220.2 ± 96.4	46.60	—
—	4200	—	—	59.2	VF	I3	—	—	—	—	—
MACS J0744.8+3927	3197	07:44:52.802	+39:27:24.41	20.2	VF	I3	0.6860	11.29	42.4 ± 10.9	24.70	—
—	3585	—	—	19.9	VF	I3	—	—	—	—	—
—	6111	—	—	49.5	VF	I3	—	—	—	—	—
MACS J1115.2+5320	3253	11:15:15.632	+53:20:03.31	8.8	VF	I3	0.4390	8.03	292.3 ± 60.5	14.30	—
—	5008	—	—	18.0	VF	I3	—	—	—	—	—
—	5350	—	—	6.9	VF	I3	—	—	—	—	—
MACS J1115.8+0129	3275	11:15:52.048	+01:29:56.56	15.9	VF	I3	0.1200	6.78	22.7 ± 4.8	1.49	—
MACS J1131.8-1955	3276	11:31:54.580	-19:55:44.54	13.9	VF	I3	0.3070	8.64	97.3 ± 23.0	17.60	—
MACS J1149.5+2223	1656	11:49:35.856	+22:23:55.02	18.5	VF	I3	0.5440	8.40	280.7 ± 39.2	21.60	—
—	3589	—	—	20.0	VF	I3	—	—	—	—	—
MACS J1206.2-0847	3277	12:06:12.276	-08:48:02.40	23.5	VF	I3	0.4400	10.21	69.0 ± 10.1	37.30	—
MACS J1311.0-0310	3258	13:11:01.665	-03:10:39.50	14.9	VF	I3	0.4940	5.60	47.4 ± 4.1	10.00	—

TABLE 1 — *Continued*


Cluster — (1)	Obs. ID — (2)	R.A. hr:min:sec (3)	Decl. ° : ' : '' (4)	Exp. Time ksec (5)	Mode — (6)	ACIS — (7)	z — (8)	$kT_X$ keV (9)	$K_0$ keV cm <sup>2</sup> (10)	$L_{bol}$ 10 <sup>44</sup> ergs s <sup>-1</sup> (11)	Notes — (12)
—	6110	—	—	63.2	VF	I3	—	—	—	—	—
MACS J1621.3+3810	3254	16:21:24.801	+38:10:08.65	9.8	VF	I3	0.4610	7.53	20.1 ± 5.4	11.50	—
—	3594	—	—	19.7	VF	I3	—	—	—	—	—
—	6109	—	—	37.5	VF	I3	—	—	—	—	—
—	6172	—	—	29.8	VF	I3	—	—	—	—	—
MACS J1931.8-2634	3282	19:31:49.656	-26:34:33.99	13.6	VF	I3	0.3520	6.97	14.6 ± 3.6	23.40	e
MACS J2049.9-3217	3283	20:49:56.245	-32:16:52.30	23.8	VF	I3	0.3254	6.98	195.8 ± 67.6	8.71	—
MACS J2211.7-0349	3284	22:11:45.856	-03:49:37.24	17.7	VF	I3	0.2700	11.30	165.5 ± 25.5	22.20	—
MACS J2214.9-1359	3259	22:14:57.467	-14:00:09.35	19.5	VF	I3	0.5026	8.80	297.7 ± 83.2	24.10	—
—	5011	—	—	18.5	VF	I3	—	—	—	—	—
MACS J2228+2036	3285	22:28:33.872	+20:37:18.31	19.9	VF	I3	0.4120	7.86	118.8 ± 39.2	18.10	—
MACS J2229.7-2755	3286	22:29:45.358	-27:55:38.41	16.4	VF	I3	0.3240	5.01	12.4 ± 2.0	9.60	—
MACS J2245.0+2637	3287	22:45:04.657	+26:38:03.46	16.9	VF	I3	0.3040	6.06	42.0 ± 6.5	9.46	—
MKW3S	900	15:21:51.930	+07:42:31.97	57.3	VF	I3	0.0450	2.18	23.9 ± 1.6	1.14	—
MKW 4	3234	12:04:27.218	+01:53:42.79	30.0	VF	S3	0.0198	2.06	6.9 ± 0.3	0.03	—
MKW 8	4942	14:40:39.633	+03:28:13.61	23.1	VF	I3	0.0270	3.29	130.7 ± 22.4	0.85	a,b
MS J0016.9+1609	520	00:18:33.503	+16:26:12.99	67.4	VF	I3	0.5410	8.94	162.1 ± 22.5	33.20	—
MS J0116.3-0115	4963	01:18:53.944	-01:00:07.54	39.3	VF	S3	0.0452	1.84	12.8 ± 31.0	-0.00	—
MS J0440.5+0204	4196	04:43:09.952	+02:10:18.70	59.4	VF	S3	0.1900	5.46	25.5 ± 7.6	2.21	—
MS J0451.6-0305	902	04:54:11.004	-03:00:52.19	44.2	F	S3	0.5386	8.90	568.1 ± 115.6	33.60	—
MS J0735.6+7421	4197	07:41:44.245	+74:14:38.23	45.5	VF	S3	0.2160	5.55	16.0 ± 2.1	7.65	—
MS J0839.8+2938	2224	08:42:55.969	+29:27:26.97	29.8	F	S3	0.1940	4.68	19.2 ± 2.9	3.13	—
MS J0906.5+1110	924	09:09:12.753	+10:58:32.00	29.7	VF	I3	0.1630	5.38	104.2 ± 14.9	4.69	—
MS J1006.0+1202	925	10:08:47.462	+11:47:36.31	29.4	VF	I3	0.2210	5.61	160.3 ± 21.3	4.81	—
MS J1008.1-1224	926	10:10:32.312	-12:39:56.80	44.2	VF	I3	0.3010	7.45	97.6 ± 41.5	8.53	—
MS J1455.0+2232	4192	14:57:15.088	+22:20:32.49	91.9	VF	I3	0.2590	4.77	16.9 ± 1.5	10.40	—
MS J2137.3-2353	4974	21:40:15.178	-23:39:40.71	57.4	VF	S3	0.3130	6.01	14.7 ± 1.9	11.40	—
MS J1157.3+5531	4964	11:59:52.295	+55:32:05.61	75.1	VF	S3	0.0810	3.28	5.9 ± 0.4	0.12	b
NGC 507	2882	01:23:39.905	+33:15:21.73	43.6	VF	I3	0.0164	1.40	0.0 ± -0.0	0.24	c
NGC 4636	3926	12:42:49.856	+02:41:15.86	74.7	VF	I3	0.0031	0.66	1.4 ± 0.1	-0.00	c
—	4415	—	—	74.4	VF	I3	—	—	—	—	—
NGC 5044	3225	13:15:23.947	-16:23:07.62	83.1	VF	S3	0.0090	1.22	2.3 ± 0.2	0.21	c
—	3664	—	—	61.3	VF	S3	—	—	—	—	—
NGC 5813	5907	15:01:11.260	+01:42:07.23	48.4	VF	S3	0.0066	0.76	1.4 ± 0.2	0.03	c
NGC 5846	788	15:06:29.289	+01:36:20.13	29.9	F	S3	0.0057	0.64	1.8 ± 0.2	0.02	c
Ophiuchus	3200	17:12:27.731	-23:22:06.74	50.5	F	S3	0.0280	11.12	8.9 ± 1.2	2.78	—
PKS 0745-191	2427	07:47:31.436	-19:17:39.78	17.9	VF	S3	0.1028	8.50	12.4 ± 0.7	18.40	—
—	508	—	—	28.0	F	S3	—	—	—	—	—
—	6103	—	—	10.3	VF	I3	—	—	—	—	—
RBS 461	4182	03:41:17.490	+15:23:54.66	23.4	VF	I3	0.0290	2.60	95.7 ± 3.0	-0.00	a,e
RBS 533	3186	04:19:38.105	+02:24:35.54	10.0	VF	I3	0.0123	1.29	2.2 ± 0.1	-0.00	—
—	3187	—	—	9.6	VF	I3	—	—	—	—	—
—	5800	—	—	44.5	VF	S3	—	—	—	—	—
—	5801	—	—	44.4	VF	S3	—	—	—	—	—
RBS 797	2202	09:47:12.971	+76:23:13.90	11.7	VF	I3	0.3540	7.68	14.0 ± 6.0	26.30	d
RX J0220.9-3829	9411	02:20:56.582	-38:28:51.21	19.9	VF	I3	0.2287	4.86	43.0 ± 6.3	-0.00	—
RX J0232.2-4420	4993	02:32:18.771	-44:20:46.68	23.4	VF	I3	0.2836	7.83	44.6 ± 12.4	18.30	—
RX J0439+0520	527	04:39:02.218	+05:20:43.11	9.6	VF	I3	0.2080	4.60	14.9 ± 2.9	3.61	—
RX J0439.0+0715	1449	04:39:00.710	+07:16:07.65	6.3	F	I3	0.2300	6.50	66.8 ± 18.5	9.44	—
—	3583	—	—	19.2	VF	I3	—	—	—	—	—
RX J0528.9-3927	4994	05:28:53.039	-39:28:15.53	22.5	VF	I3	0.2632	7.89	72.8 ± 13.8	13.10	—
RX J0647.7+7015	3196	06:47:50.029	+70:14:49.66	19.3	VF	I3	0.5840	9.07	225.1 ± 47.1	26.50	—
—	3584	—	—	20.0	VF	I3	—	—	—	—	—
RX J0819.6+6336	2199	08:19:26.007	+63:37:26.53	14.9	F	S3	0.1190	3.87	20.7 ± 14.3	1.12	—
RX J1000.4+4409	9421	10:00:32.024	+44:08:39.69	18.5	VF	I3	0.1540	3.42	27.7 ± 4.4	-0.00	—
RX J1022.1+3830	6942	10:22:10.034	+38:31:23.54	41.5	VF	S3	0.0491	3.04	51.6 ± 9.8	-0.00	—
RX J1130.0+3637	6945	11:30:02.789	+36:38:08.26	49.4	VF	S3	0.0600	2.02	29.9 ± 2.3	-0.00	—
RX J1320.2+3308	6941	13:20:14.650	+33:08:33.06	38.6	VF	S3	0.0366	1.01	8.8 ± 0.7	-0.00	e
RX J1347.5-1145	3592	13:47:30.593	-11:45:10.05	57.7	VF	I3	0.4510	10.88	12.4 ± 20.6	100.00	—
—	507	—	—	10.0	F	S3	—	—	—	—	—
RX J1504.1-0248	5793	15:04:07.415	-02:48:15.70	39.2	VF	I3	0.2150	8.00	13.1 ± 0.9	34.90	—
RX J1532.9+3021	1649	15:32:53.781	+30:20:58.72	9.4	VF	I3	0.3450	5.44	16.9 ± 1.8	20.80	—
—	1665	—	—	10.0	VF	S3	—	—	—	—	—
RX J1720.1+2638	4361	17:20:09.941	+26:37:29.11	25.7	VF	I3	0.1640	6.37	21.0 ± 1.9	11.50	—
RX J1720.2+3536	3280	17:20:16.953	+35:36:23.63	20.8	VF	I3	0.3913	5.65	24.0 ± 3.4	13.00	—
—	6107	—	—	33.9	VF	I3	—	—	—	—	—
—	7225	—	—	2.0	VF	I3	—	—	—	—	—
RX J1852.1+5711	5749	18:52:08.815	+57:11:42.63	29.8	VF	I3	0.1094	3.44	18.7 ± 8.2	-0.00	—
RX J2129.6+0005	552	21:29:39.944	+00:05:18.83	10.0	VF	I3	0.2350	5.91	21.1 ± 3.7	12.70	—
SC 1327-312	4165	13:29:47.748	-31:36:23.54	18.4	VF	I3	0.0531	3.53	64.6 ± 9.9	3.16	—
Sersic 159-03	1668	23:13:58.764	-42:43:34.70	9.9	VF	S3	0.0580	2.65	10.4 ± 0.7	1.10	—
SS2B153	3243	10:50:26.125	-12:50:41.76	29.5	VF	S3	0.0186	0.80	1.1 ± 0.2	-0.00	—
UGC 3957	8265	07:40:58.335	+55:25:38.30	7.9	VF	I3	0.0341	2.96	12.9 ± 1.0	-0.00	—
ZWCL 1215	4184	12:17:41.708	+03:39:15.81	12.1	VF	I3	0.0750	6.62	163.2 ± 35.6	3.52	—
ZWCL 1358+6245	516	13:59:50.526	+62:31:04.57	54.1	F	S3	0.3280	10.66	20.7 ± 3.2	12.50	—

TABLE 1 — *Continued*

Cluster — (1)	Obs. ID — (2)	R.A. hr:min:sec (3)	Decl. ° : ' : '' (4)	Exp. Time ksec (5)	Mode — (6)	ACIS — (7)	z — (8)	$kT_X$ keV (9)	$K_0$ keV cm <sup>2</sup> (10)	$L_{bol}$ 10 <sup>44</sup> ergs s <sup>-1</sup> (11)	Notes — (12)
ZWCL 1742	8267	17:44:14.515	+32:59:29.68	8.0	VF	I3	0.0757	4.40	23.8 ± 1.6	-0.00	—
ZWCL 1953	1659	08:50:06.677	+36:04:16.16	24.9	F	I3	0.3800	7.37	194.5 ± 56.6	17.30	—
ZWCL 3146	909	10:23:39.735	+04:11:08.05	46.0	F	I3	0.2900	7.48	11.4 ± 2.0	29.90	—
ZWCL 7160	543	14:57:15.158	+22:20:33.85	9.9	F	I3	0.2578	4.53	21.1 ± 3.1	10.30	—
Zwicky 2701	3195	09:52:49.183	+51:53:05.27	26.9	VF	S3	0.2100	5.21	39.7 ± 3.9	5.24	—
ZwCl 857.9+2107	7897	09:00:36.835	+20:53:40.36	9.0	VF	I3	0.2350	12.10	24.2 ± 5.0	-0.00	e

NOTE. — Col. (1) Cluster name; col. (2) CXC CDA Observation Identification Number; col. (3) R.A. of cluster center; col. (4) Decl. of cluster center; col. (5) exposure time; col. (6) observing mode; col. (7) CCD location of cluster center; col. (8) redshift; col. (9) average cluster temperature; col. (10) core entropy measured in this work; col. (11) cluster bolometric luminosity; and col. (12) notes are as follows: (a) – cluster analyzed using the best-fit  $\beta$ -model for the surface brightness profiles (discussed in §3.2); (b) – clusters with complex surface brightness of which only the central regions were used in fitting  $K(r)$ ; (c) – cluster only used during analysis of the *HIFLUGCS* sub-sample (discussed in §5.4); (d) – cluster with central AGN removed during analysis (discussed in §3.5); (e) – cluster with central compact source removed during analysis (discussed in §3.5);

TABLE 2  
SUMMARY OF  $\beta$ -MODEL FITS



Cluster — (1)	$S_{01}$ $10^{-6}$ cts/s/asec <sup>2</sup> (2)	$r_{c1}$ " (3)	$\beta_1$ — (4)	$S_{02}$ $10^{-6}$ cts/s/asec <sup>2</sup> (5)	$r_{c2}$ " (6)	$\beta_2$ — (7)	D.O.F. — (8)	$\chi^2_{\text{red}}$ — (9)
Abell 119	$4.93 \pm 0.73$	$39.1 \pm 15.3$	$0.34 \pm 0.07$	$3.52 \pm 0.96$	$735.2 \pm 479.4$	$1.27 \pm 1.27$	52	1.76
Abell 160	$2.32 \pm 0.27$	$53.4 \pm 11.1$	$0.57 \pm 0.12$	$1.29 \pm 0.22$	$284.0 \pm 52.2$	$0.74 \pm 0.10$	90	1.18
Abell 193	$25.18 \pm 0.75$	$72.7 \pm 4.9$	$0.40 \pm 0.01$	—	—	—	100	1.26
Abell 400	$4.66 \pm 0.09$	$151.3 \pm 6.4$	$0.42 \pm 0.01$	—	—	—	96	0.57
Abell 1240	$1.58 \pm 0.07$	$247.9 \pm 46.9$	$1.01 \pm 0.22$	—	—	—	58	1.58
Abell 1736	$3.81 \pm 0.56$	$55.6 \pm 16.1$	$0.42 \pm 0.12$	$2.49 \pm 0.47$	$1470.0 \pm 87.2$	$5.00 \pm 0.73$	35	1.58
Abell 2125	$3.50 \pm 0.20$	$26.0 \pm 4.9$	$0.49 \pm 0.05$	$1.02 \pm 0.13$	$159.9 \pm 9.2$	$1.32 \pm 0.16$	35	0.33
Abell 2255	$8.38 \pm 0.15$	$222.7 \pm 9.8$	$0.62 \pm 0.02$	—	—	—	94	1.45
Abell 2319	$47.39 \pm 0.61$	$128.8 \pm 3.1$	$0.49 \pm 0.01$	—	—	—	92	1.67
Abell 2462	$8.19 \pm 1.43$	$60.8 \pm 9.6$	$0.64 \pm 0.11$	$1.87 \pm 0.25$	$762.7 \pm 39.1$	$5.00 \pm 0.87$	67	1.54
Abell 2631	$20.55 \pm 1.01$	$66.0 \pm 4.0$	$0.73 \pm 0.03$	—	—	—	58	1.15
Abell 3376	$4.21 \pm 0.09$	$125.5 \pm 5.6$	$0.40 \pm 0.01$	—	—	—	98	1.42
Abell 3391	$10.65 \pm 0.31$	$132.3 \pm 7.9$	$0.48 \pm 0.01$	—	—	—	84	1.86
Abell 3395	$6.85 \pm 0.67$	$90.9 \pm 6.7$	$0.49 \pm 0.03$	—	—	—	38	0.96
MKW 8	$7.71 \pm 0.62$	$25.2 \pm 2.5$	$0.32 \pm 0.01$	$1.51 \pm 0.08$	$1124.0 \pm 64.1$	$5.00 \pm 0.40$	88	0.65
RBS 461	$12.84 \pm 0.34$	$102.2 \pm 4.1$	$0.52 \pm 0.01$	—	—	—	84	1.56

NOTE. — Col. (1) Cluster name; col. (2) central surface brightness of first component; col. (3) core radius of first component; col. (4)  $\beta$  parameter of first component; col. (5) central surface brightness of second component; col. (6) core radius of second component; col. (7)  $\beta$  parameter of second component; col. (8) model degrees of freedom; and col. (9) reduced chi-squared statistic for best-fit model.



TABLE 3  
M. DONAHUE'S  $H\alpha$  OBSERVATIONS.

Cluster	Telescope	$z$	$N_H/H\alpha$	$H\alpha$ Flux $10^{-15}$ ergs/s/cm <sup>2</sup>
—	—	—	—	
Abell 85	PO	0.0558	2.67	0.581
Abell 119	LC	0.0442	—	<0.036
Abell 133	LC	0.0558	—	0.88
Abell 496	LC	0.0328	2.50	2.90
Abell 1644	LC	0.0471	—	1.00
Abell 1650	LC	0.0843	—	<0.029
Abell 1689	LC	0.1843	—	<0.029
Abell 1736	LC	0.0338	—	<0.026
Abell 2597	PO	0.0854	0.85	29.7
Abell 3112	LC	0.0720	2.22	2.66
Abell 3158	LC	0.0586	—	<0.036
Abell 3266	LC	0.0590	1.62	<0.027
Abell 4059	LC	0.0475	3.60	2.22
Cygnus A	PO	0.0561	1.85	28.4
EXO 0422-086	LC	0.0397	—	<0.031
Hydra A	LC	0.0522	0.85	13.4
PKS 0745-191	LC	0.1028	1.02	10.4

NOTE. — The abbreviation “PO” denotes observations taken on the 5 m Hale Telescope at the Palomar Observatory, USA, while “LC” are observations taken on the DuPont 2.5 m telescope at the Las Campanas Observatory, Chile. Upperlimits for  $H\alpha$  fluxes are  $3\sigma$ .

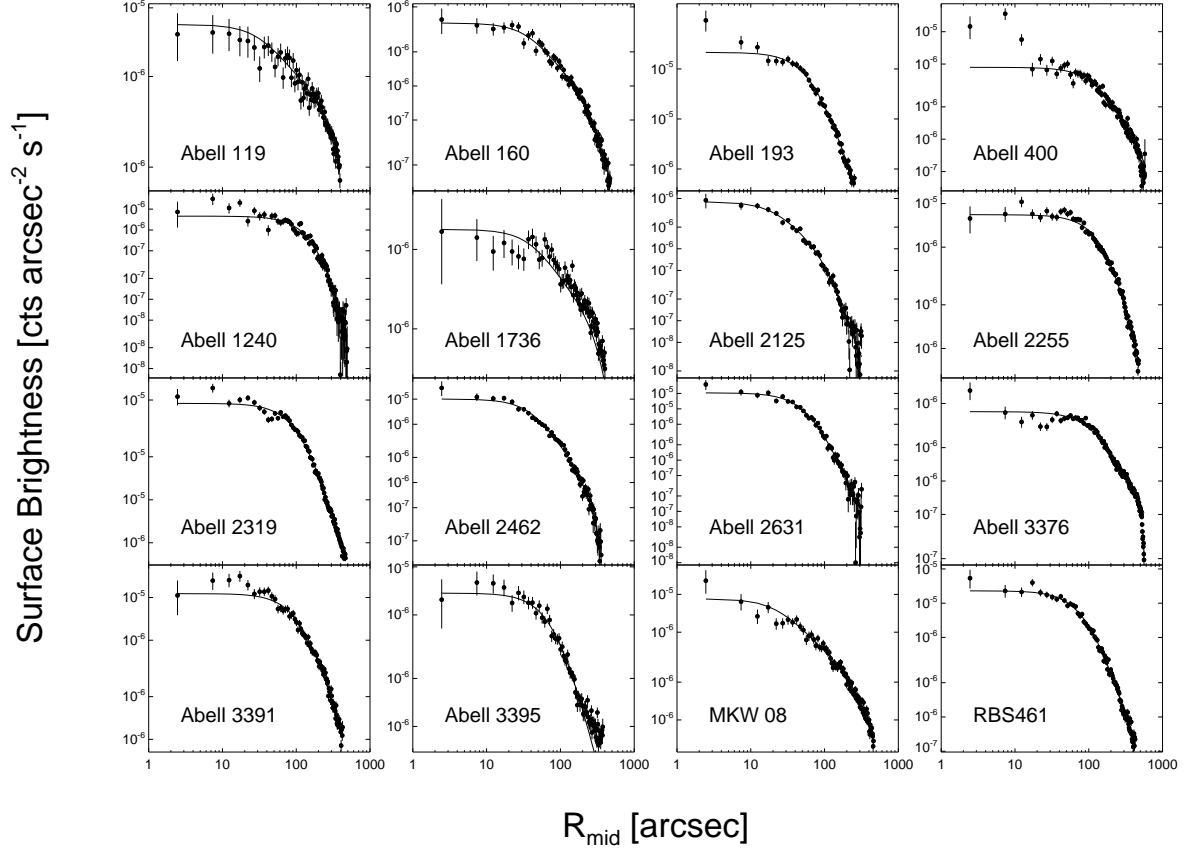


FIG. 1.— Presented here is a montage of normalized surface brightness profiles for the clusters requiring a  $\beta$ -model fit (discussed in §3.3). The best-fit  $\beta$ -model for each cluster is overplotted as a dashed line. The discrepancy between the data and best-fit model for some clusters results from the presence of a compact X-ray source at the center of the cluster. These cases are discussed in Appendix A.



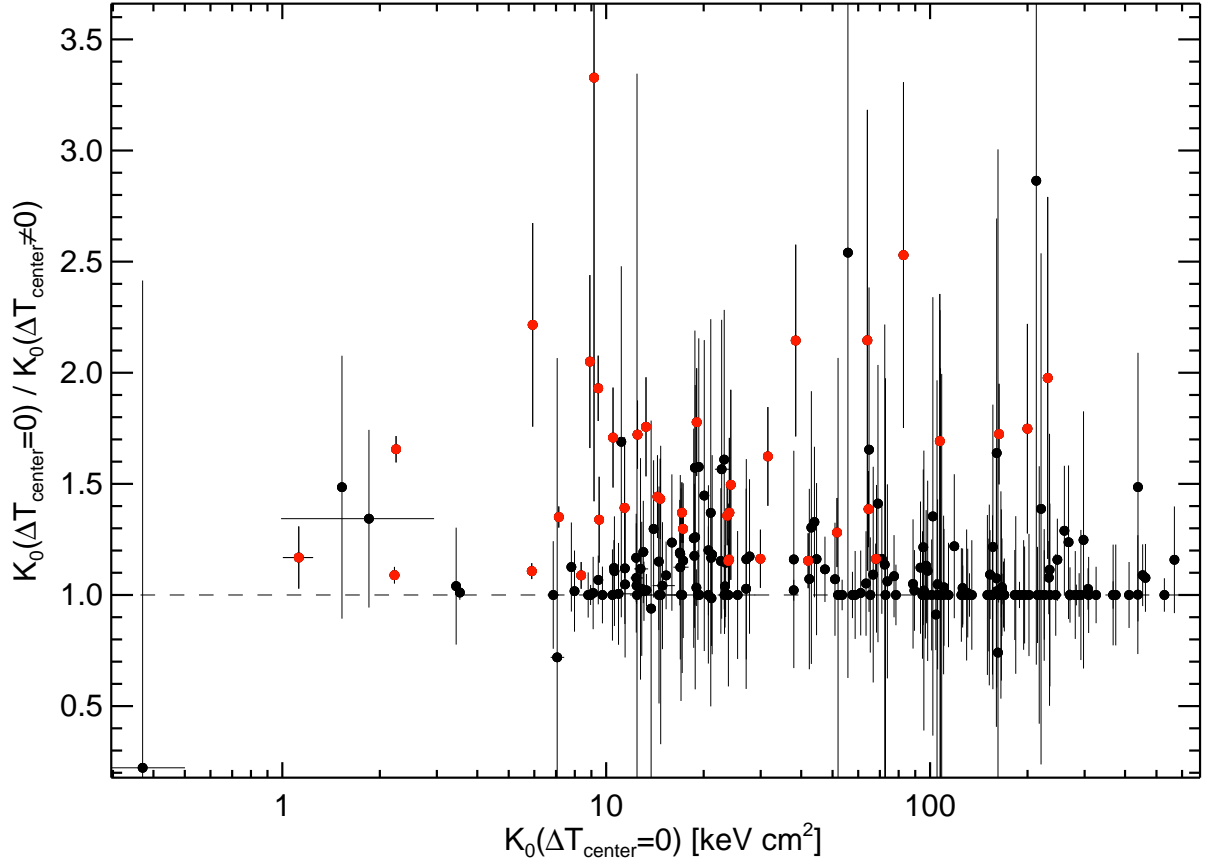


FIG. 2.— Plotted here is the ratio of best-fit  $K_0$  for the two treatments of central temperature interpolation (see §3.1): 1) temperature is free to decline across the central density bins ( $\Delta T_{\text{center}} = 0$ ) and 2) the temperature across the central density bins is isothermal ( $\Delta T_{\text{center}} \neq 0$ ). Red points are clusters where the  $K_0$  ratio is inconsistent with unity. All of these clusters also have steep temperature gradients.



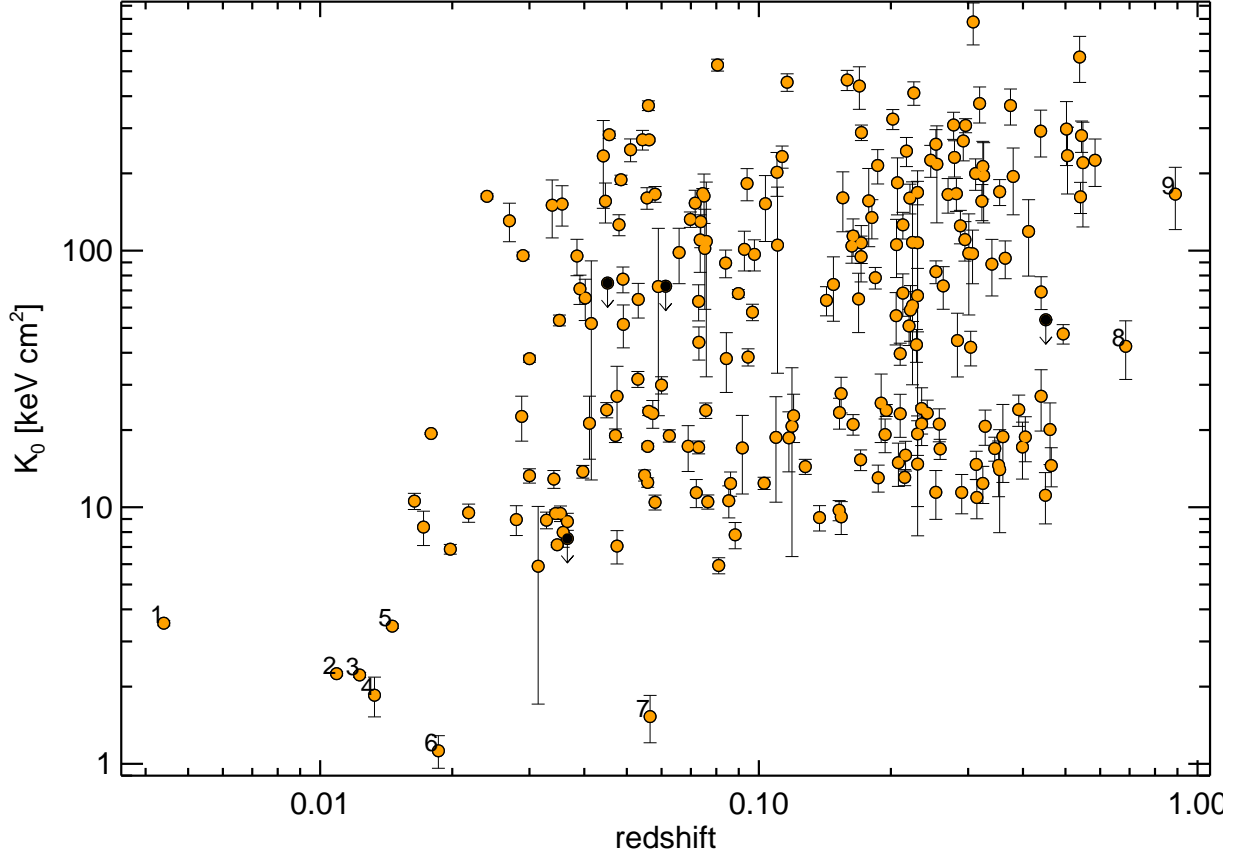


FIG. 3.— Plot of best-fit  $K_0$  versus redshift. Some clusters have  $K_0$  error bars smaller than the point. The clusters with upper-limits (black points with downward arrows) are: A2151, AS0405, MS 0116.3-0115, and RX J1347.5-1145. The numerically labeled clusters are: (1) M87, (2) Centaurus Cluster, (3) RBS 533, (4) HCG 42, (5) HCG 62, (6) SS2B153, (7) A1991, (8) MACS0744.8+3927, and (9) CL J1226.9+3332. For CLJ1226, Maughan et al. (2007) found best-fit  $K_0 = 132 \pm 24 \text{ keV cm}^2$  which is not significantly different from our value of  $K_0 = 166 \pm 45 \text{ keV cm}^2$ . The lack of  $K_0 < 10 \text{ keV cm}^2$  clusters at  $z > 0.1$  is most likely the result of insufficient angular resolution (see §4.2).

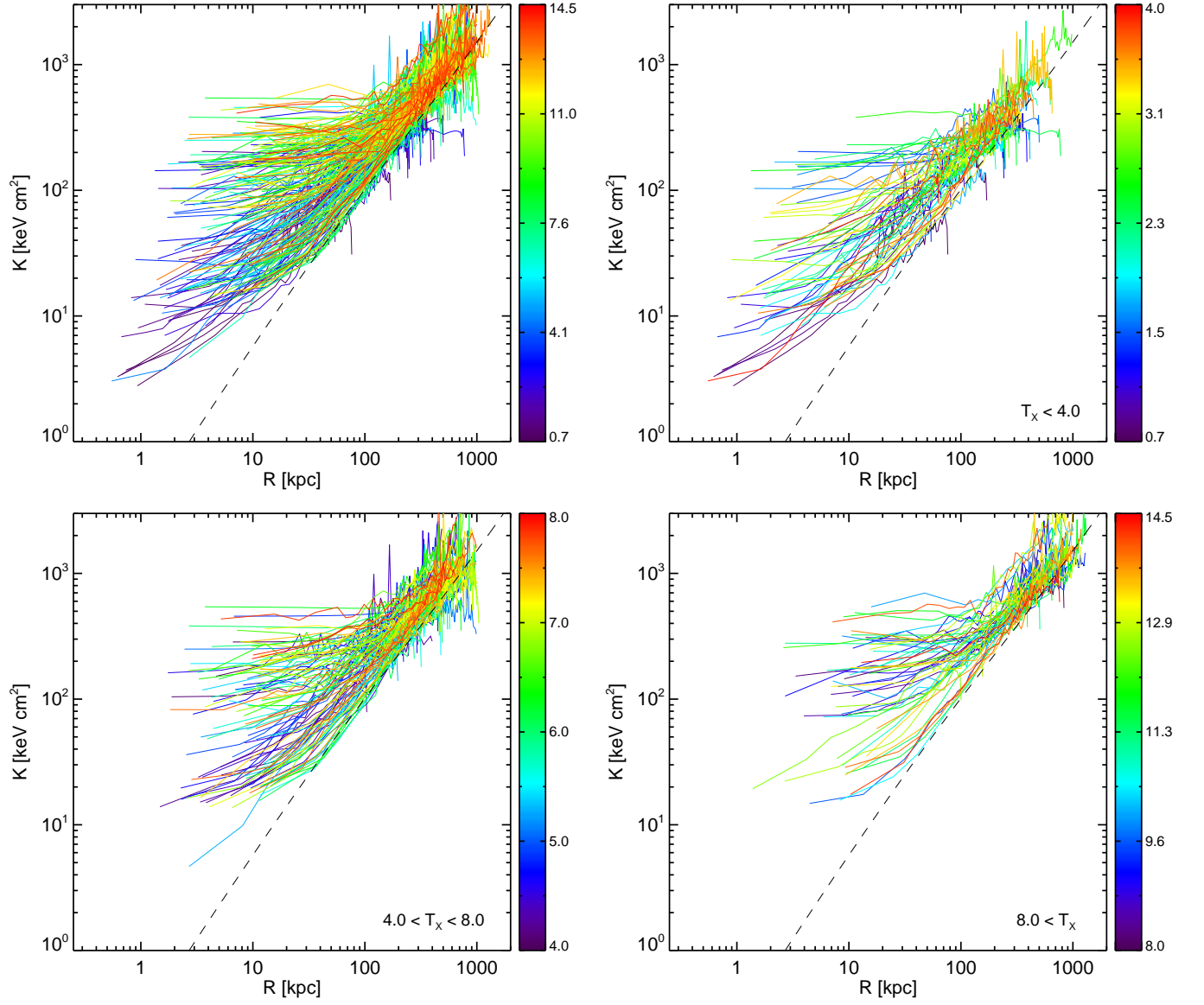


FIG. 4.— Shown here is a montage of composite plots of entropy profiles for varying cluster temperature ranges. Profiles are color-coded based on the cluster temperature. Units of the color bars are keV. *Top left:* This panel contains all the entropy profiles in our study. *Top right:* Clusters with  $kT < 4$  keV. *Bottom left:* Clusters with  $4 \text{ keV} < kT < 8 \text{ keV}$ . *Bottom right:* Clusters with  $kT > 8$  keV. Note that while the dispersion of core entropy for each temperature range is large, as the  $kT$  range increases so to does the mean core entropy.

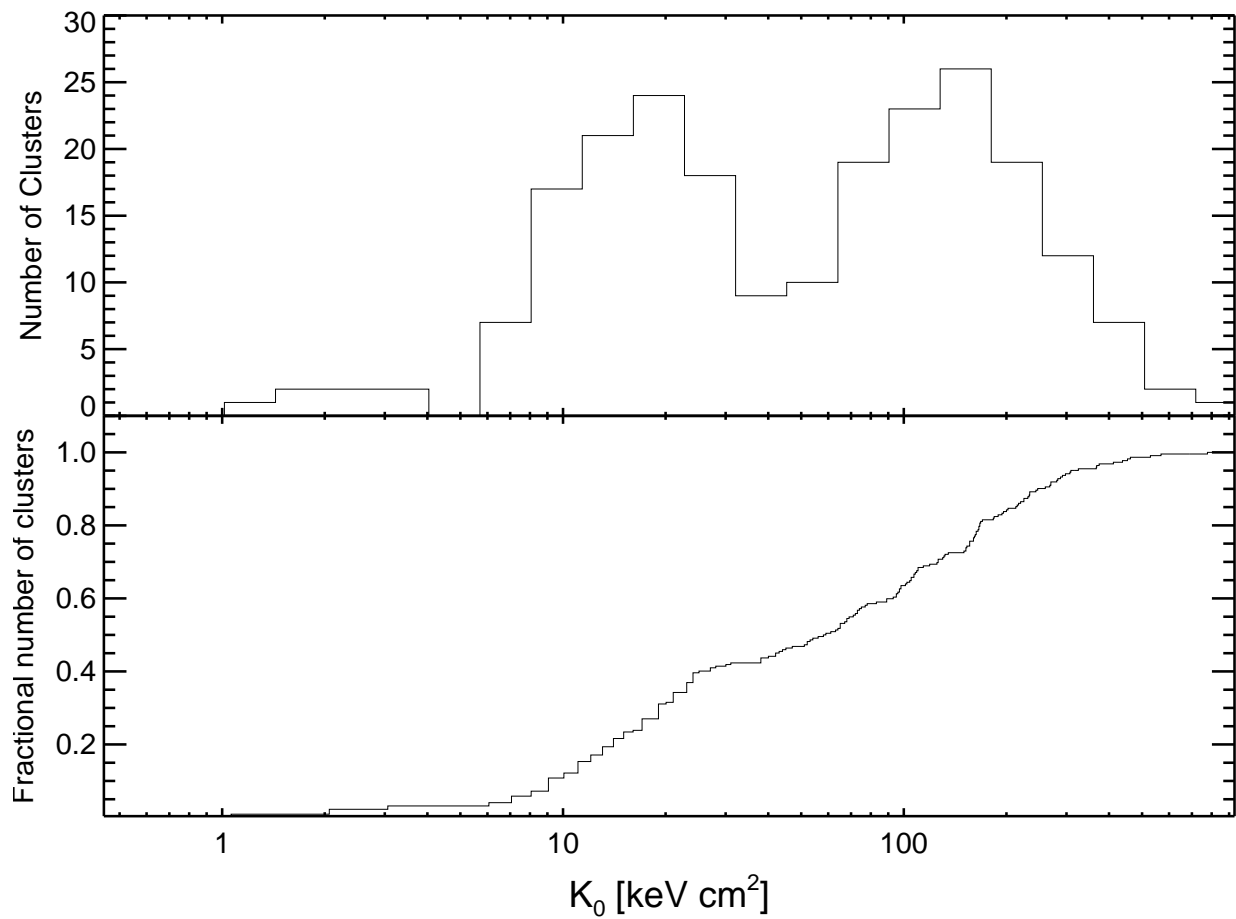


FIG. 5.— Presented here are a histogram of best-fit  $K_0$  for all the clusters in *ACCEPT* (top panel), and the cumulative distribution of  $K_0$  values for the full sample (bottom panel). The top panel is logarithmically binned using bin widths of 0.15 in log space. The distinct bimodality in  $K_0$  is present in both distributions, which would not be seen if it were an artifact of the histogram binning.

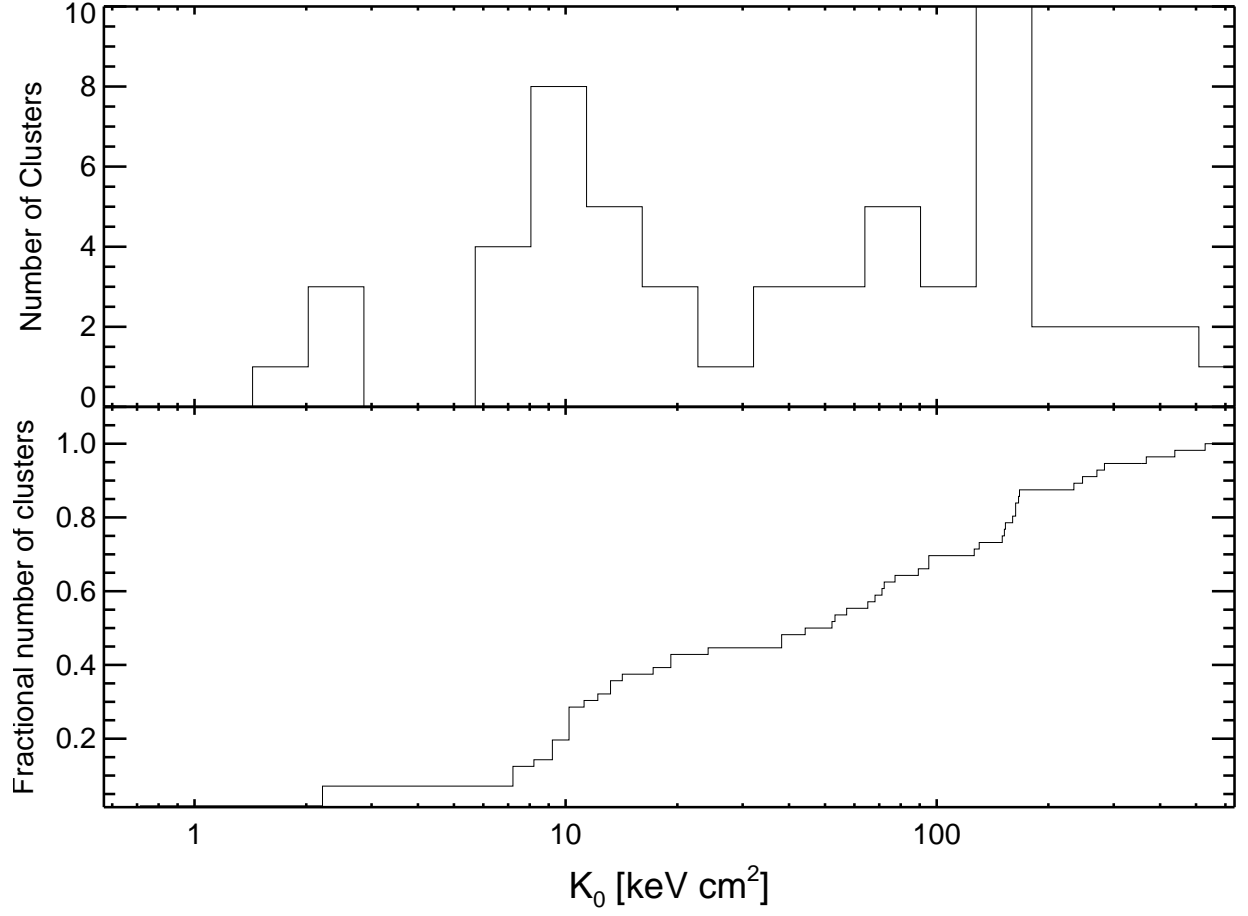


FIG. 6.— Presented here are the histogram of best-fit  $K_0$  values (top panel) and cumulative distribution of  $K_0$  values (bottom panel) for the *HIFLUGCS* subsample. The top panel is logarithmically binned using bin widths of 0.15 in log space. The distinct bimodality seen in the full *ACCEPT* sample is also present in the *HIFLUGCS* subsample and shares the same gap of  $K_0 \approx 40$ – $60$  keV cm<sup>2</sup>. That bimodality is present in both samples is strong evidence it is not a result of an unknown archival bias.

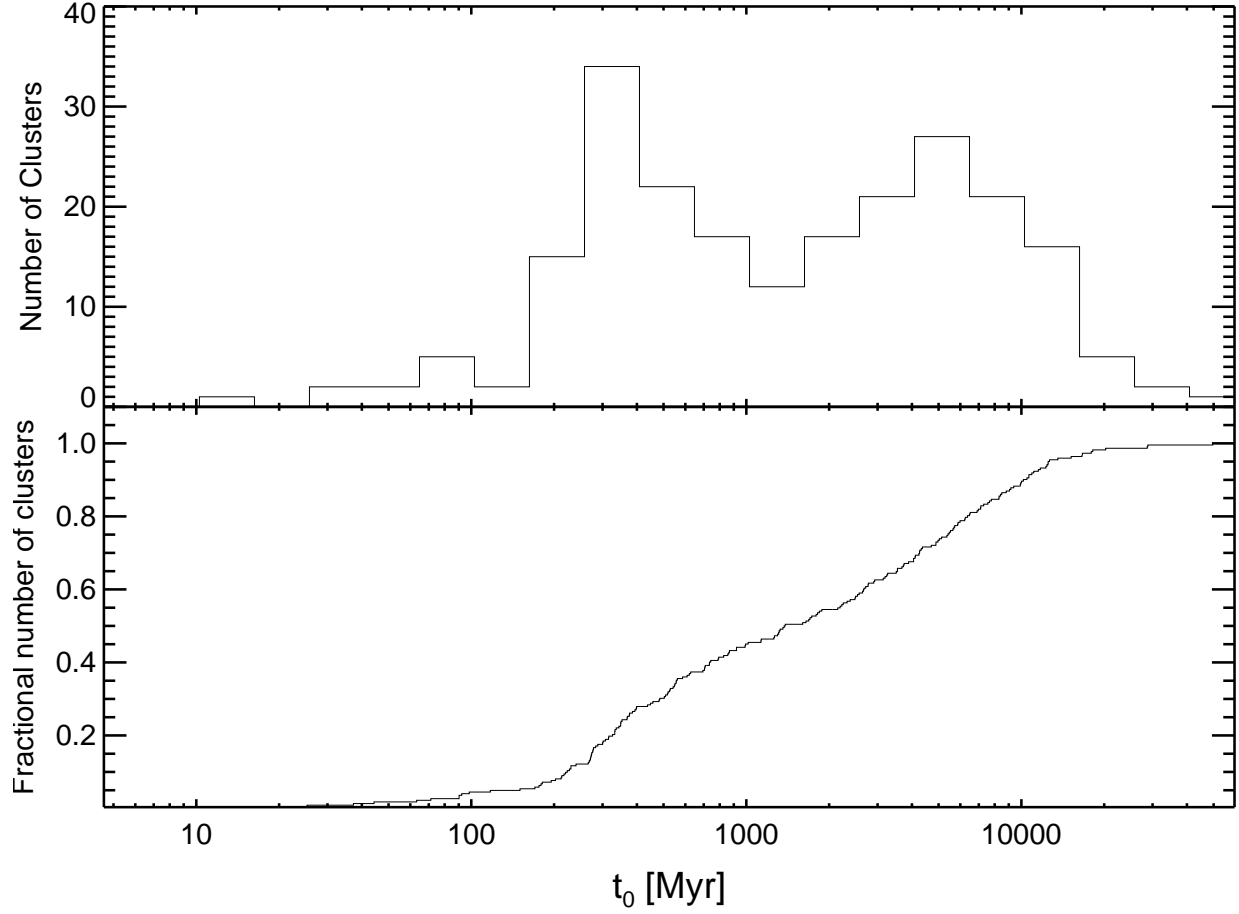


FIG. 7.— Plotted is the log-binned histogram (top panel) and cumulative distribution of best-fit core cooling times,  $t_0$ , for all the clusters in *ACCEPT*. The bimodality we observe in the  $K_0$  distribution is also present in best-fit cooling times. But, after scaling  $K_0$  into cooling time, we find the population gaps vary by  $\sim 0.3$  Gyrs with scaled-entropy having the shorter of the two. This indicates a cluster having a core cooling time shorter than 1 Gyr is most likely not the defining criterion for bimodality. This cooling time bimodality is also seen in the *HIFLUGCS* subsample.